

AD-A037 739

STANFORD UNIV CALIF RADIO ASTRONOMY INST
FINE STRUCTURE ON THE SUN AT 2.8 CM.(U)
DEC 76 C J GREBENKEMPER

F/G 3/2

UNCLASSIFIED

AFOL-TR-76-0307

F19628-74-C-0053
NL

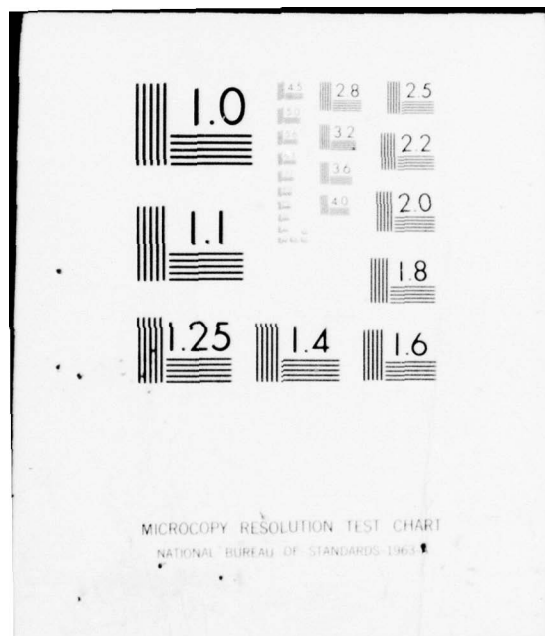
1 of 1
AD
A037739



END

DATE
FILMED

4-77



ADA037739

AFGL-TR-76-0307

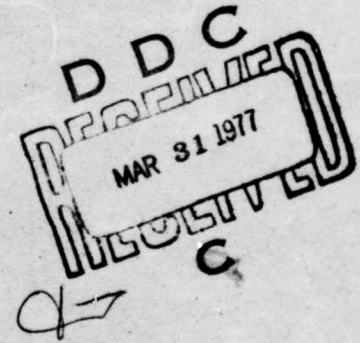
FINE STRUCTURE ON THE SUN AT 2.8 CM

C. John Grebenkemper

Radio Astronomy Institute
Stanford University
Stanford, California 94305

16 December 1976

Final Report
1 September 1973 through 30 September 1976



Approved for public release; distribution unlimited.

AIR FORCE GEOPHYSICS LABORATORY
AIR FORCE SYSTEMS COMMAND
UNITED STATES AIR FORCE
HANSCOM AFB, MASSACHUSETTS 01731

AD NO. _____
DDC FILE COPY

Qualified requestors may obtain additional copies from the Defense Documentation Center. All others should apply to the National Technical Information Service.

UNCLASSIFIED

SECURITY CLASSIFICATION OF THIS PAGE (When Data Entered)

REPORT DOCUMENTATION PAGE		READ INSTRUCTIONS BEFORE COMPLETING FORM
1. REPORT NUMBER AFGL-TR-76-0307	2. GOVT ACCESSION NO.	3. RECIPIENT'S CATALOG NUMBER
4. TITLE (and Subtitle) FINE STRUCTURE ON THE SUN AT 2.8 CM.		5. TYPE OF REPORT & PERIOD COVERED Scientific - Final 9/1/73 - 9/30/76
7. AUTHOR(s) C. John Grebenkemper		6. PERFORMING ORG. REPORT NUMBER
9. PERFORMING ORGANIZATION NAME AND ADDRESS Radio Astronomy Institute Stanford University Stanford, California 94305		8. CONTRACT OR GRANT NUMBER(s) F19628-74-C-0053
11. CONTROLLING OFFICE NAME AND ADDRESS Air Force Geophysics Laboratory Hanscom AFB, Massachusetts 01731 Monitor/R. B. Dunn/PHS		10. PROGRAM ELEMENT, PROJECT, TASK AREA & WORK UNIT NUMBERS 7649-07-01 62101F 687649
14. MONITORING AGENCY NAME & ADDRESS (if different from Controlling Office) Final scientific rept. 1 Sep 73 - 30 Sep 76		12. REPORT DATE 16 December 1976
16. DISTRIBUTION STATEMENT (of this Report) Approved for public release; distribution unlimited. 1267p.		13. NUMBER OF PAGES 63
17. DISTRIBUTION STATEMENT (of the abstract entered in Block 20, if different from Report)		15. SECURITY CLASS. (of this report) UNCLASSIFIED
18. SUPPLEMENTARY NOTES		15a. DECLASSIFICATION/DOWNGRADING SCHEDULE
19. KEY WORDS (Continue on reverse side if necessary and identify by block number) solar active region solar flares solar radio emission solar five-minute oscillations Stanford interferometer		
20. ABSTRACT (Continue on reverse side if necessary and identify by block number) More than 400 hours of observations of the 2.8 cm solar radio emission were obtained with the Stanford interferometer. The observations were divided into two categories: the emission of the quiet sun and the emission from active regions. The observations of the quiet sun reveal emission from fine structure in addition to the thermal emission component. This fine structure is time varying. One-dimensional power spectra of the variations show that the power decreases as f^{-2} , and there is no significant peak in the power spectra near the observed optical five-minute oscillations. → next page		

DD FORM 1 JAN 73 1473

EDITION OF 1 NOV 65 IS OBSOLETE

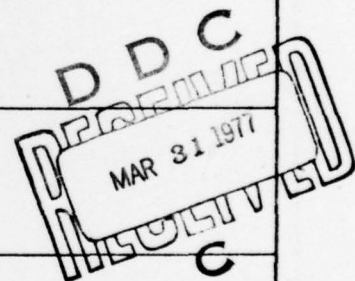
UNCLASSIFIED

F to the -2 power

SECURITY CLASSIFICATION OF THIS PAGE (When Data Entered)

400503

LB



UNCLASSIFIED

SECURITY CLASSIFICATION OF THIS PAGE(When Data Entered)

cont → Four radio bursts were observed during observations of solar active regions. One of these bursts was classified as a simple burst, and the other three were post-burst events. Two of the post-burst events were measured for their circular polarization. The instantaneous one-dimensional resolution of the interferometer shows that the simple burst could have been in the same location as an H-alpha sub-flare which occurred at the same time. The observations of the post-burst events show that they were primarily an enhancement of the pre-existing S-component emission. The percentage of circularly polarized radiation remained essentially unchanged throughout each of the events. A model is proposed for explaining the post-burst observations.



UNCLASSIFIED

SECURITY CLASSIFICATION OF THIS PAGE(When Data Entered)

ii ii

TABLE OF CONTENTS

1. INSTRUMENTATION	1
2. QUIET SUN OBSERVATIONS	6
3. EQUATORIAL COORDINATES OF A SOURCE ON THE SUN	21
4. MAXIMUM ENTROPY SOLUTIONS	30
5. DESCRIPTION OF SOLAR RADIO BURSTS	36
6. INTERPRETATION OF THE RADIO BURSTS	57
7. RECOMMENDATIONS FOR FUTURE WORK	61
8. REFERENCES	63

ACCESSION NO.	
NTIS	NTIS SYMBOL
DOC	DOC SYMBOL
DATE RECEIVED	DATE RECEIVED
PREPARED BY	
PROJECT OR PROGRAM	
REMARKS	
<div style="display: flex; justify-content: space-between;"> INITIALS DATE </div>	
A	

1. INSTRUMENTATION

The Stanford Interferometer is located in the foothills behind Stanford University. The interferometer consists of five 60 foot parabolic reflectors arranged in a minimum redundancy configuration along an East-West baseline. The five antennas can be combined into 10 two-element interferometers, nine of which are measuring different spatial coordinates. The output of each of these is referred to as the complex visibility, and the length of time that each of these outputs is averaged is referred to as the integration time. Due to noise considerations of the sampling process it is necessary to monitor the smallest spacing for an integral number of fringes. This means that the minimum integration time is $16.8/[\cos(\delta)\cos(h)]$ seconds or multiples thereof, where δ is the source declination and h is the source hour-angle. This effect limits our maximum time resolution to about 17 seconds on the meridian near $\delta = 0$. More detailed descriptions of the instrument may be found in Bracewell et al. [1973] and D'Addario [1974]. Some of the operating characteristics of the interferometer are listed in Table 1.

There are two methods of controlling the signal gain of the five antennas: the automatic level control (ALC) mode and the manual mode. Both of these modes of operation have been used for observing the sun. In the manual mode the signal gain is set manually. The gain may be

TABLE I. STANFORD FIVE-ELEMENT INTERFEROMETER

Operating Frequency:	10.69 GHz
Operating Wavelength:	2.804 cm
IF Bandwidth:	10-70 mHz, double sideband
Single Dish Diameter:	18.3 m
Single Dish Beamwidth:	7' full-width to half-power
Minimum Antenna Spacing:	22.9 m, 815 wavelengths
Maximum Antenna Spacing:	205.7 m, 7337 wavelengths
Sensitivity:	$0.4 \times 10^{-26} \text{ Wm}^{-2} \text{ Hz}^{-1}$ for a one-minute integration on one channel
Noise Temperature:	<400 K
Feedhorns:	Linear, rotatable to 0°, 60°, 90°, and 120° electric vector east of north
Feedhorn Rotation Rate:	7.5°/s
Maximum Fringe Rate:	0.53 Hz
Minimum Sampling Interval:	17 s with no horn rotation; 30 s with computer controlled horn rotation
Array Geocentric Coordinates:	Latitude +37° 23' 55" Longitude +122° 11' 22"

changed in steps of 10 dB by insertion of calibrated attenuators. For observing the astronomical calibrators 0 dB attenuation is used. The largest attenuation that has been used on the sun is 30 dB. The 30 dB attenuation would allow observing compact sources on the sun with strengths as great as 100 solar flux units (1 solar flux unit = $10^{-22} \text{ W m}^{-2} \text{ Hz}^{-1}$). The manual mode does not compensate for drifts in the instrumental gain. The major components of these gain changes are a 10% change associated with the switching of the delay lines and the drift of the electronics gain with temperature which may be as large as 50%. The delay line gain changes are corrected to about 1% when processing the raw data. The electronics gain drift is compensated for by observing a calibrator source every few hours. However, this still leaves an estimated residual gain error of about 10%. This residual error limits the accuracy with which we can reconstruct the original source brightness distribution. The manual mode has been used to observe solar active regions; changes in the observed signal due to radio bursts are faithfully recorded and absolute amplitudes are better known than when observing in the ALC mode.

In the ALC mode of operation the gain of each IF amplifier is electronically controlled so that the output stays at a constant power. When observing an astronomical source the noise contributed by the front end receivers is much greater than the noise from the radio source. The automatic level control keeps the gain constant if the system noise temperature remains constant. However, the system noise temperature varies about 10% with temperature causing a corresponding gain drift.

Using a sufficient number of calibrators this gain variation can be reduced to a few per cent. When observing the sun, the 12 000 K signal from the sun is greater than the 400 K front end noise by more than an order of magnitude. If the signal from the sun remains constant, the ALC circuit acts as if it were an automatic gain control circuit and compensates for any gain changes to better than 1%. This is the mode used to observe the quiet sun. The thermal emission of the quiet sun has a strength of 20 solar flux units within the 7' single dish beamwidth, while the varying part of the quiet sun has a strength on the order of 0.01 solar flux unit. Thus the assumption that the solar signal is constant is indeed a good assumption. However, the ALC mode suffers from two disadvantages. One is that it cannot be used to look at strong sources which are time-varying such as solar active regions. The other is that the absolute amplitudes of the complex visibilities are not well determined. As the antennas are pointed away from an astronomical calibrator to the sun, the gain of the system is reduced by about 15 dB. The exact magnitude of this reduction cannot be accurately measured at present.

Each antenna has a linearly polarized feedhorn that may be rotated under remote control to positions of 0° or 90° (electric vector N-S or E-W). The on-site computer controls the orientation of the feedhorns. It takes a maximum of 12 seconds to rotate from one set of orientations to another set. Morris et al. [1964] have computed the response of a two-element interferometer with arbitrary feedhorn orientations as:

$$\begin{aligned}
R(t) = \frac{1}{2}k\{ & I[\cos(\phi_1 - \phi_2)\cos(\theta_1 - \theta_2) + i \sin(\phi_1 - \phi_2)\sin(\theta_1 + \theta_2)] \\
& + Q[\cos(\phi_1 + \phi_2)\cos(\theta_1 + \theta_2) + i \sin(\phi_1 + \phi_2)\sin(\theta_1 - \theta_2)] \\
& + U[\sin(\phi_1 + \phi_2)\cos(\theta_1 + \theta_2) + i \cos(\phi_1 + \phi_2)\sin(\theta_1 - \theta_2)] \\
& + V[\cos(\phi_1 - \phi_2)\sin(\theta_1 + \theta_2) + i \sin(\phi_1 - \phi_2)\cos(\theta_1 - \theta_2)] \} \quad (1)
\end{aligned}$$

where k is a term describing the fringe rate of an interferometer, I , Q , U and V are the Stokes parameters, ϕ denotes the orientation of the major axis of the polarization ellipse to the ℓ -axis of the coordinate system defining the Stokes parameters, and θ denotes the ellipticity given by $\theta = \tan^{-1} \mu$, where μ is the axial ratio. For the Stanford array, $\theta = 0$, because of the linear feedhorns, and ϕ may take values of 0° or 90° . Taking this into account and reducing the form to that of the calibrated complex visibilities measured by a two-element interferometer, the complex visibility may be written as:

$$V = V_I \cos(\phi_1 - \phi_2) + V_Q \cos(\phi_1 + \phi_2) + V_U \sin(\phi_1 + \phi_2) + i V_V \sin(\phi_1 - \phi_2) \quad (2)$$

where V_I , V_Q , V_U , V_V are the visibilities due to each of the four Stokes parameters. For every antenna pair there are four possible combinations of the 0° and 90° feedhorn orientations. These are 0-0, 90-90, 0-90, and 90-0, where the feedhorn orientations are for the east and west antennas of each pair. Inserting the appropriate values for ϕ_1 and ϕ_2 in equation (2) we then obtain for the four combinations mentioned:

$$\begin{aligned}
V_{0-0} &= V_I + V_Q \\
V_{90-90} &= V_I - V_Q \\
V_{0-90} &= V_U - i V_V \\
V_{90-0} &= V_U + i V_V
\end{aligned} \tag{3}$$

From these four measurements we can then calculate the visibilities of the Stokes parameters:

$$\begin{aligned}
V_I &\approx \frac{1}{2}(V_{0-0} + V_{90-90}) \\
V_Q &\approx \frac{1}{2}(V_{0-0} - V_{90-90}) \\
V_U &\approx \frac{1}{2}(V_{0-90} + V_{90-0}) \\
V_V &= \frac{i}{2}(V_{0-90} - V_{90-0})
\end{aligned} \tag{4}$$

The five antennas of the Stanford interferometer are combined to create 10 antenna pairs, of which 9 yield independent measurements. A minimum of 6 integrations is required to obtain all four Stokes parameters for every antenna pair. The I and Q components alone could be measured in two integrations, and the U and V components alone could be measured in four integrations. Including time to rotate the feedhorns, the interferometer has a time resolution of 30 seconds per integration or 3 minutes per data point when observing all four Stokes parameters.

2. QUIET SUN OBSERVATIONS

The current lack of solar activity has made the present time an ideal one for observing the quiet sun and its associated phenomena. While

there have been some observations at or near 2.8 cm [Kundu, 1974b; Lang, 1974], they have all suffered from either lack of resolution or insufficient coverage in the u-v plane to reconstruct the observed source distribution. We have conducted observations of the quiet sun with the Stanford interferometer on June 26 and December 9, 1974, and March 11 and 19, 1975. To gain more insight into instrumental effects we have also observed the moon, the galaxy M42, the quasi-stellar object 3C273, and a region of the sky containing no radio sources.

We shall present the results of these observations by two types of plots. The first type is a perspective plot of the interferometer one-dimensional scans versus time. Each scan spans a distance of 4 arc-minutes and is separated from the next scan by 20 seconds of time. The intensity scale of each plot is shown by a vertical line which is labeled in astronomical flux units per arc-second (1 astronomical flux unit = $10^{-26} \text{ W m}^{-2} \text{ Hz}^{-1}$). The second type of plot is the power spectrum of the temporal variations of the observed flux. These plots represent the average power spectrum across the entire field of view presented in the perspective plots. The intensity scaling is in arbitrary units of power; however, each plot is in the same arbitrary units.

The perspective plots of the blank sky and the galactic source M42 are shown in Figures 1 and 2. The blank sky shows essentially random variations of the flux as time progresses. The M42 perspective plot shows the one-dimensional outline of the radio source with the random fluctuations due to receiver noise superimposed on top of the source.

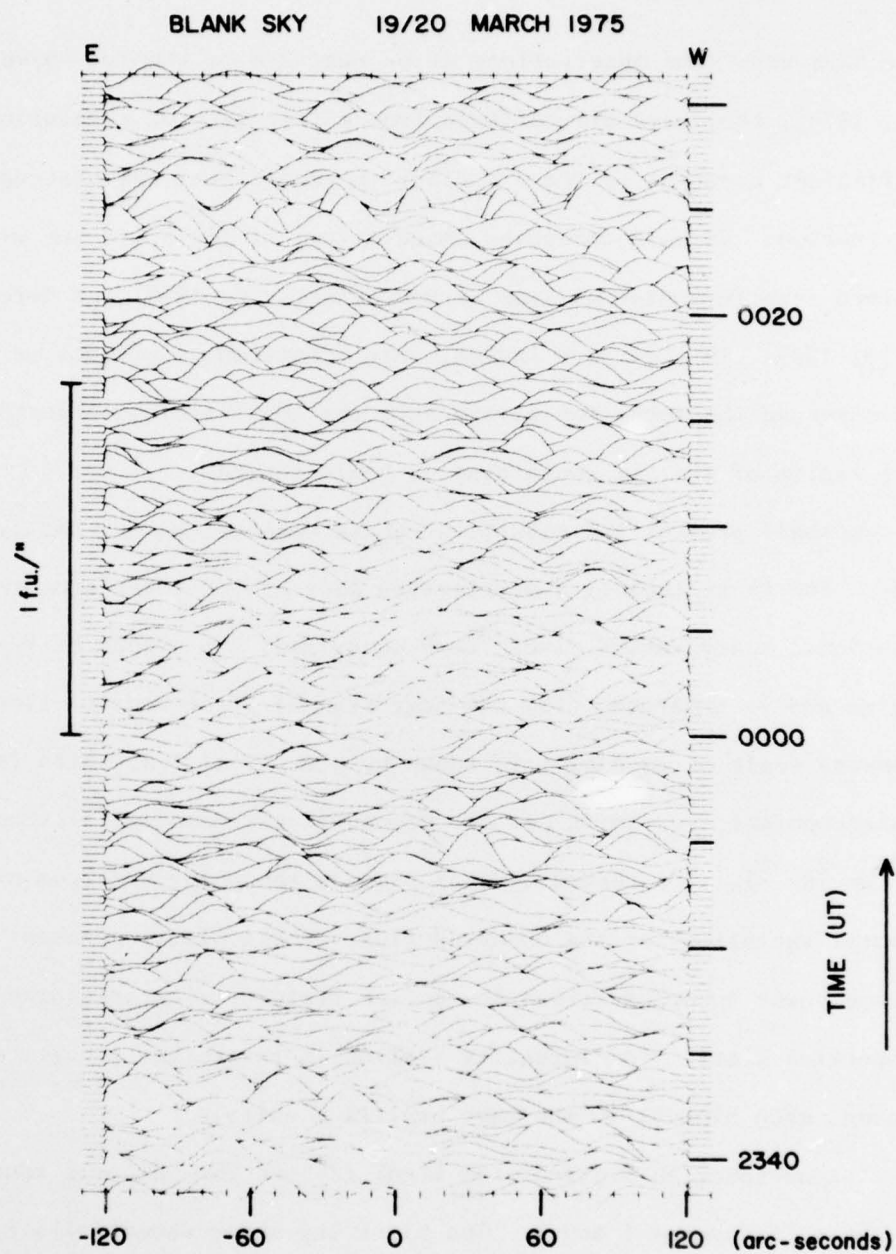


FIG. 1. Perspective plot of blank sky. No radio sources are contained within the field of view. $1 \text{ f.u.} = 10^{-26} \text{ Wm}^{-2} \text{ Hz}^{-1}$.

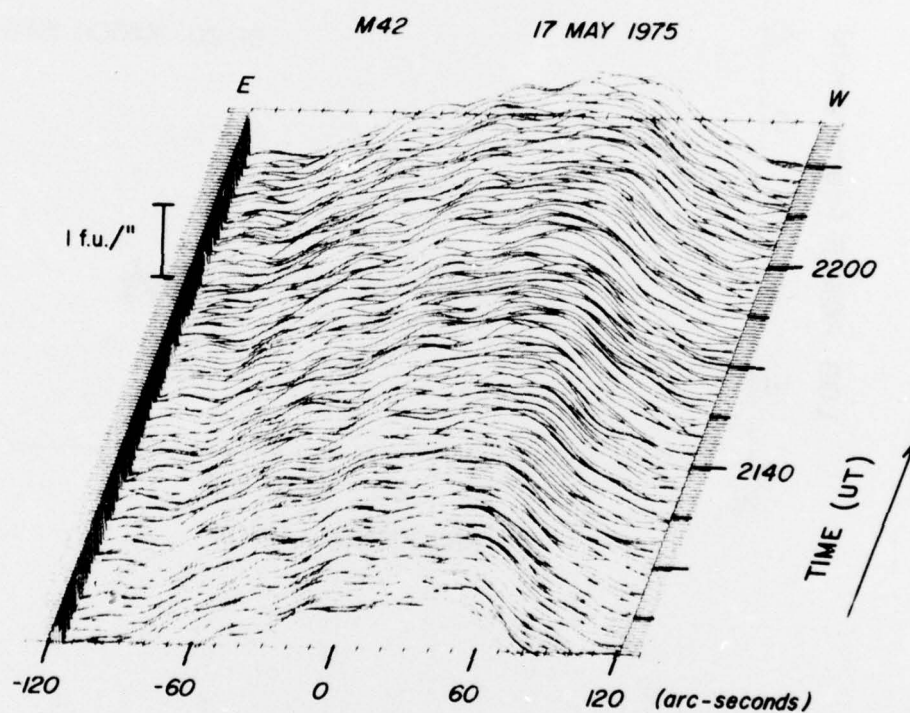


FIG. 2. Perspective plot of the galaxy M42. 1 f.u. = $10^{-26} \text{ Wm}^{-2} \text{ Hz}^{-1}$.

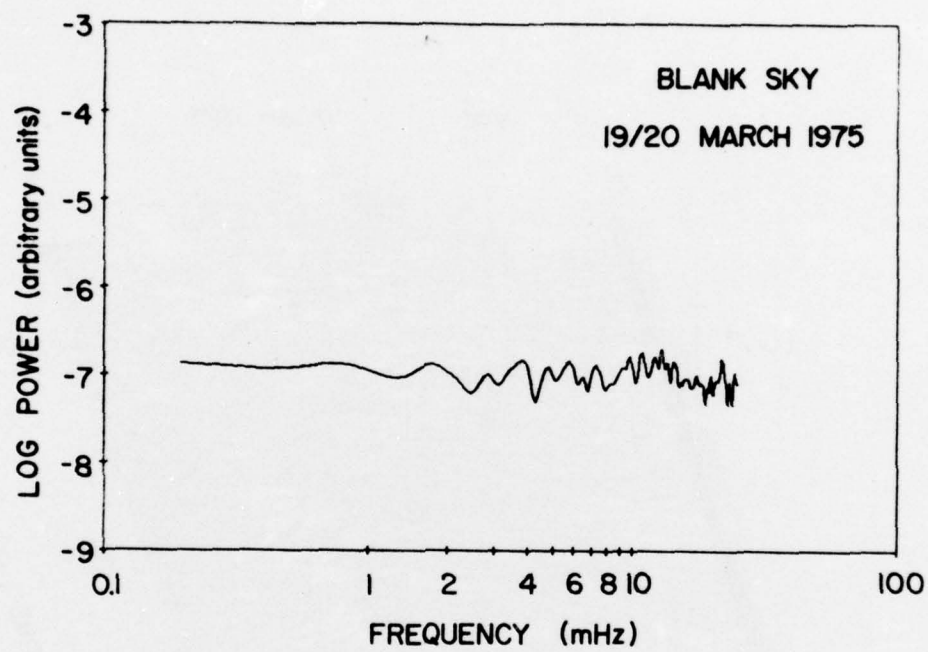


FIG. 3. Power spectrum of blank sky.

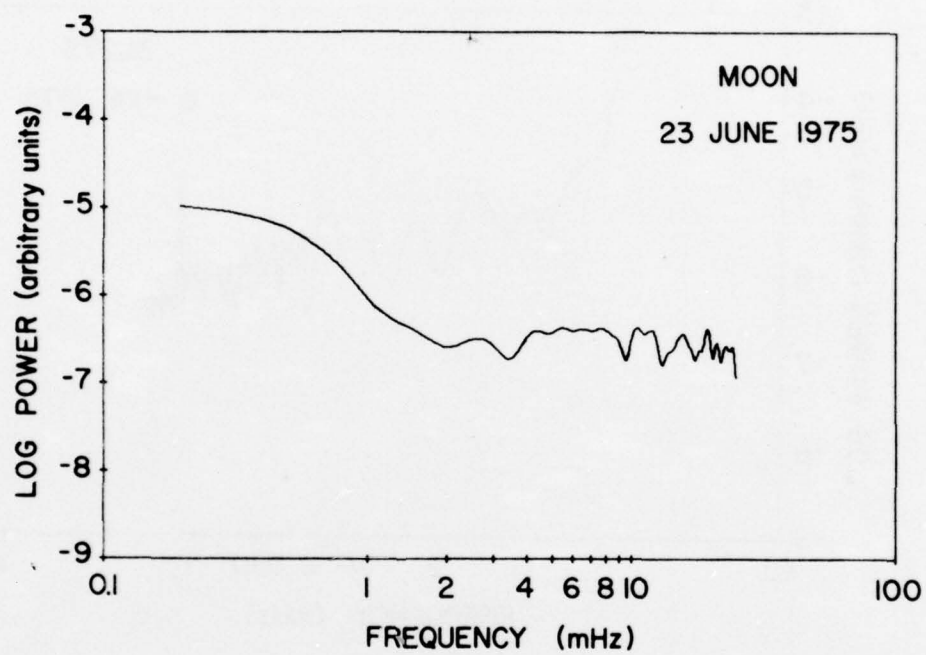


FIG. 4. Power spectrum of the moon.

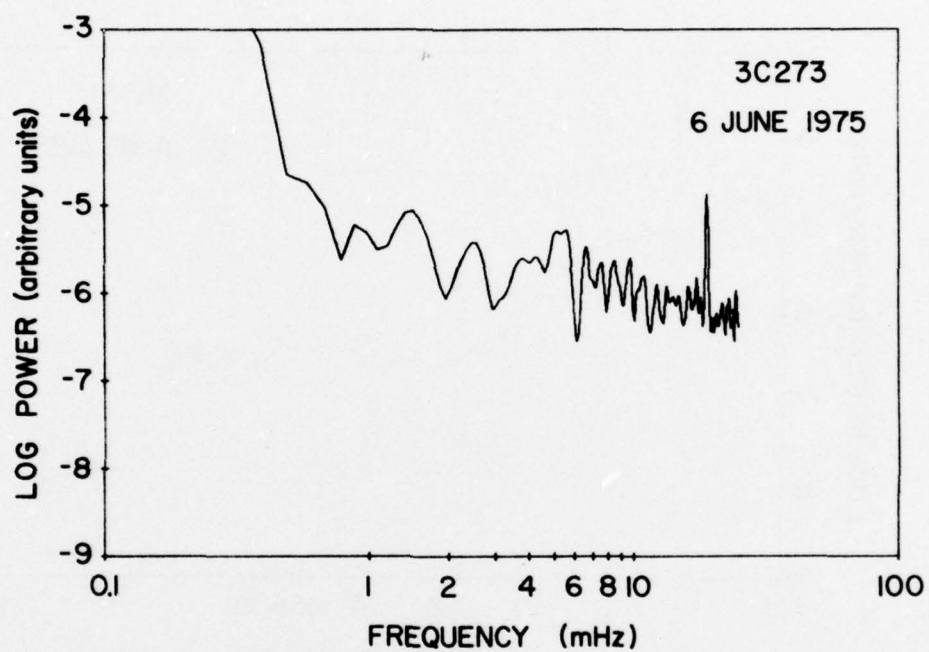


FIG. 5. Power spectrum of quasi-stellar object 3C273. The prominent peak at 16 mHz is due to the switching of the interferometer delay lines.

The noise fluctuations are on the same order of magnitude as in the blank sky data. The power spectra of the blank sky, the moon, and 3C273 are shown in Figures 3, 4 and 5. The narrow peak at a frequency of 16 mHz, which is especially prominent in the 3C273 data, is due to the switching of the interferometer delay lines. The switching, which is done once every 50 seconds, introduces small gain changes in the interferometer. Several of the solar spectra exhibit this 16 mHz peak. The increase of the power spectra at frequencies below 1 mHz is due to the finite number of data points taken in one run. For analysis of the data we shall concentrate on the frequencies between 1 and 15 mHz. All the spectra can be fit well by a curve of the power law type, f^n , which on the log (power) vs. log(frequency) plots appears as a straight line with slope n . In the following we shall quote the values obtained for n for each of the sources we observed.

On all of the non-solar sources, the power spectra are essentially flat, ranging from a slope of 0 for the blank sky to -0.5 for 3C273. None of these sources show any periodicity above the random fluctuations in the spectra. From theoretical considerations we expect each of these sources to show a flat power spectrum with no periodicity. The magnitude of all of these power spectra is 3 orders of magnitude below the solar power spectra. From these non-solar observations we conclude that there should be no instrumental effects showing up in the solar spectra in the range of 1 to 15 mHz.

Figures 6 through 11 show the perspective plots followed by the power spectra for solar observations on 9 December 1974, 11 March 1975, and 19

March 1975. The data taken on 26 June 1974 is omitted because of its poor quality due to instrumental problems. All of the data was taken at the center of the solar disk. The sunspot, calcium plage, and 2 cm radio data are taken from *Solar Geophysical Data*.

On 9 December 1974 there were no visible sunspots or sources of 2 cm radio emission on the disk and the nearest calcium plage was 7' from the solar center. The perspective plot for this date shows a number of individual sources whose lifetime is greater than one hour. The apparent motion of some of the sources is due to the rotation of the interferometer's one-dimensional scans with respect to the sun. With the exception of the delay line switching effect, the power spectrum shows no prominent peaks, and has a slope of -2.

On 11 March 1975, McMath Region 13527 is located 2' north of the disk center. However, there are no sunspots associated with the calcium plage. A single dish scan with the Stanford array was unable to detect any sources with a flux greater than 0.1 solar flux unit. The perspective plot is similar in nature to the December plot. Since the sun is near a declination of 0° , there is no apparent rotation of the interferometer's scans. The power spectrum shows no prominent peaks except for the delay line switching peak. The slope is -1.9.

On March 19, 1975 there were no sunspots or calcium plages within 10' of the disk center. The 2 cm radio emission showed no sources at all. The perspective plot shows considerably smaller amplitudes than the previous two plots. Near the end of the data run, the sources decrease further in amplitude. The power spectrum shows no prominent peaks and has a slope of about -1.6.

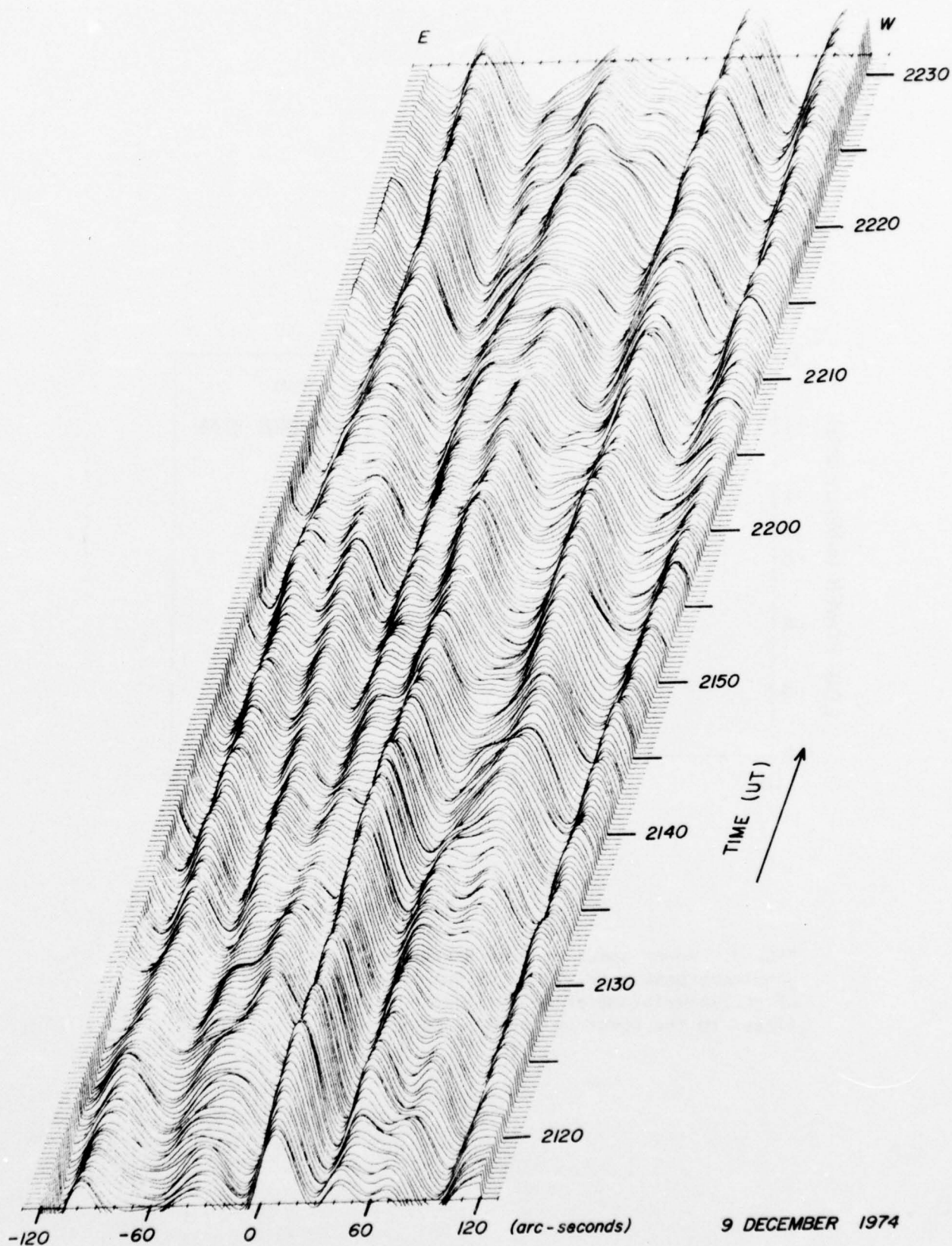


FIG. 6. Perspective plot of the sun on 9 December 1974. The interferometer was pointed at the center of the solar disk. The apparent motion of some of the radio sources is due to the rotation of the axis of the one-dimensional scans.

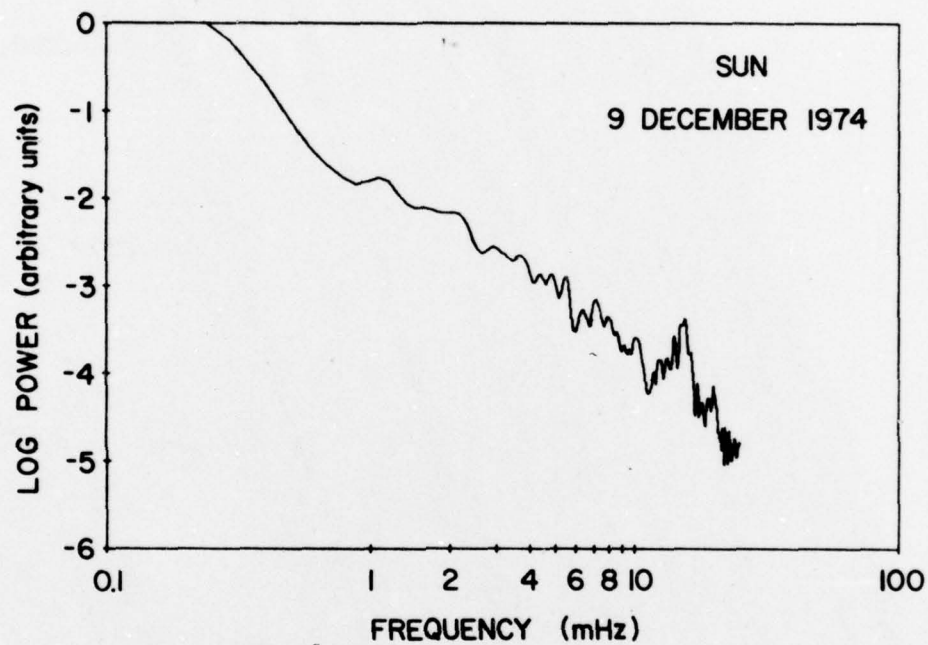


FIG. 7. Power spectrum from 9 December 1974. The prominent peak near 16 mHz is due to the switching of the interferometer delay lines. A straight line fitted to the spectrum has a slope of -2.0.

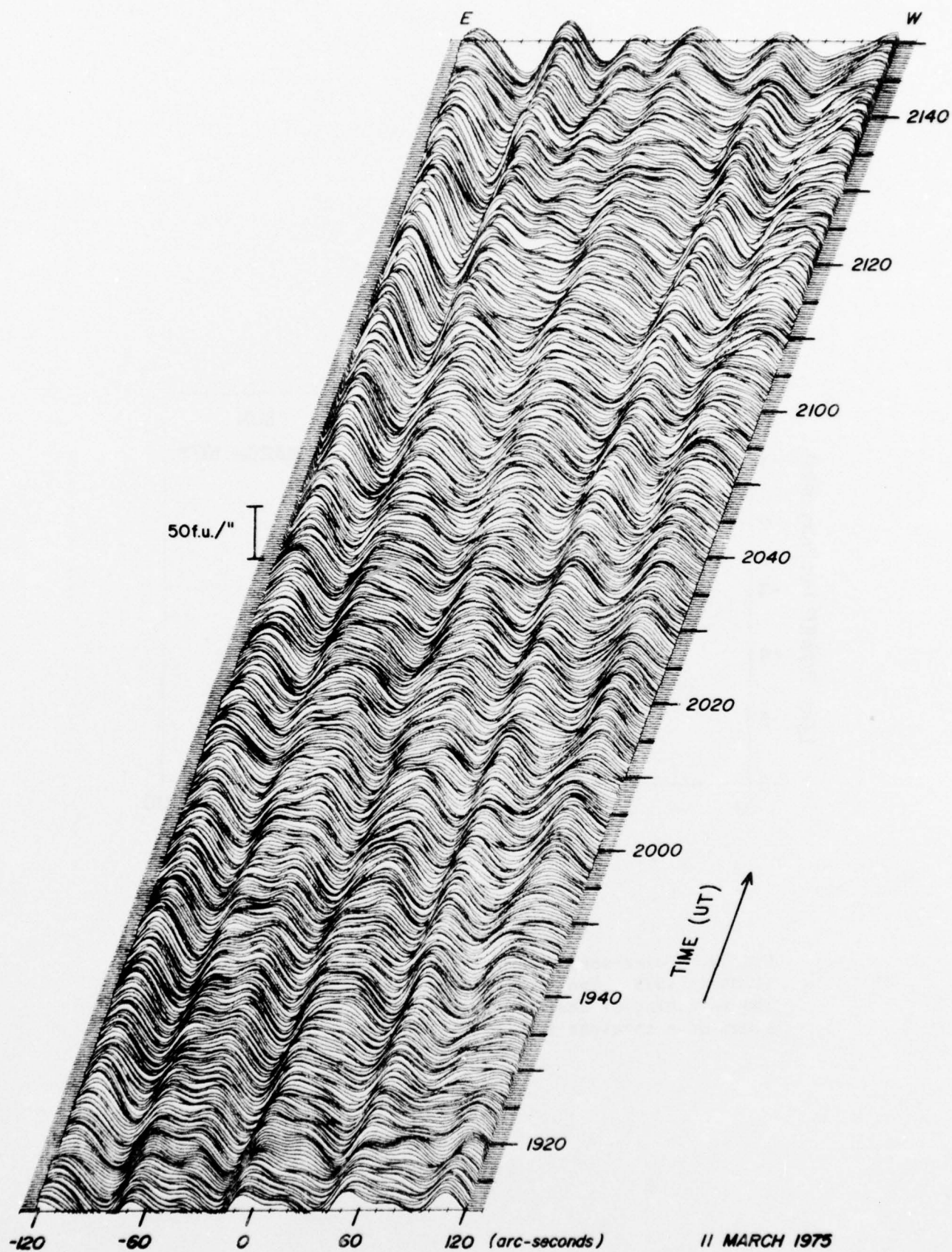


FIG. 8. Perspective plot of the center of the solar disk on 11 March 1975. 1 f.u. = $10^{-26} \text{ km}^{-2} \text{ Hz}^{-1}$.

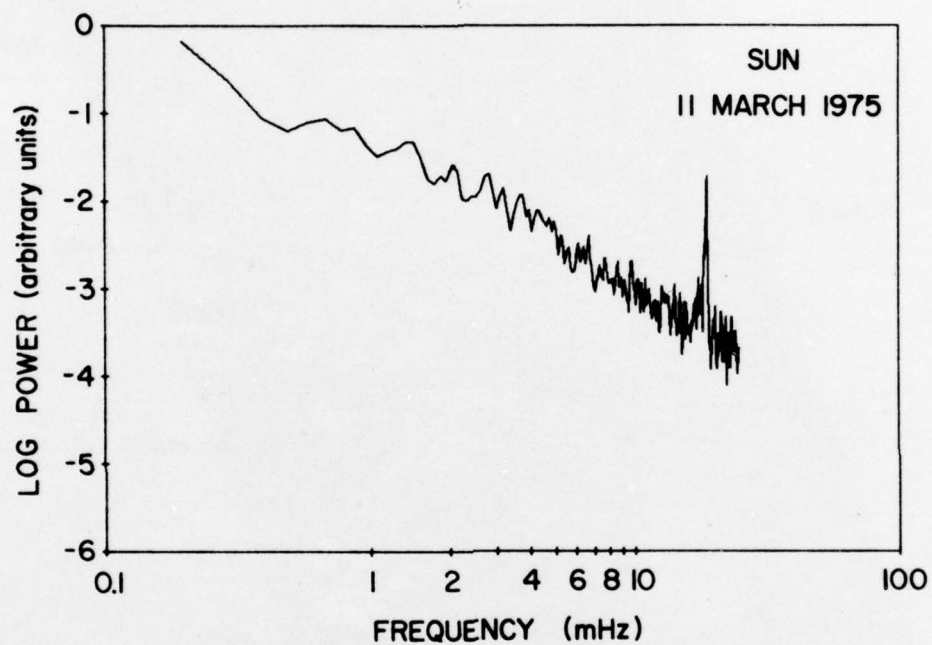


FIG. 9. Power spectrum of the solar observation on 11 March 1975. The prominent peak near 16 mHz is due to the switching of the interferometer delay lines. The slope of a straight line fit is -1.9.

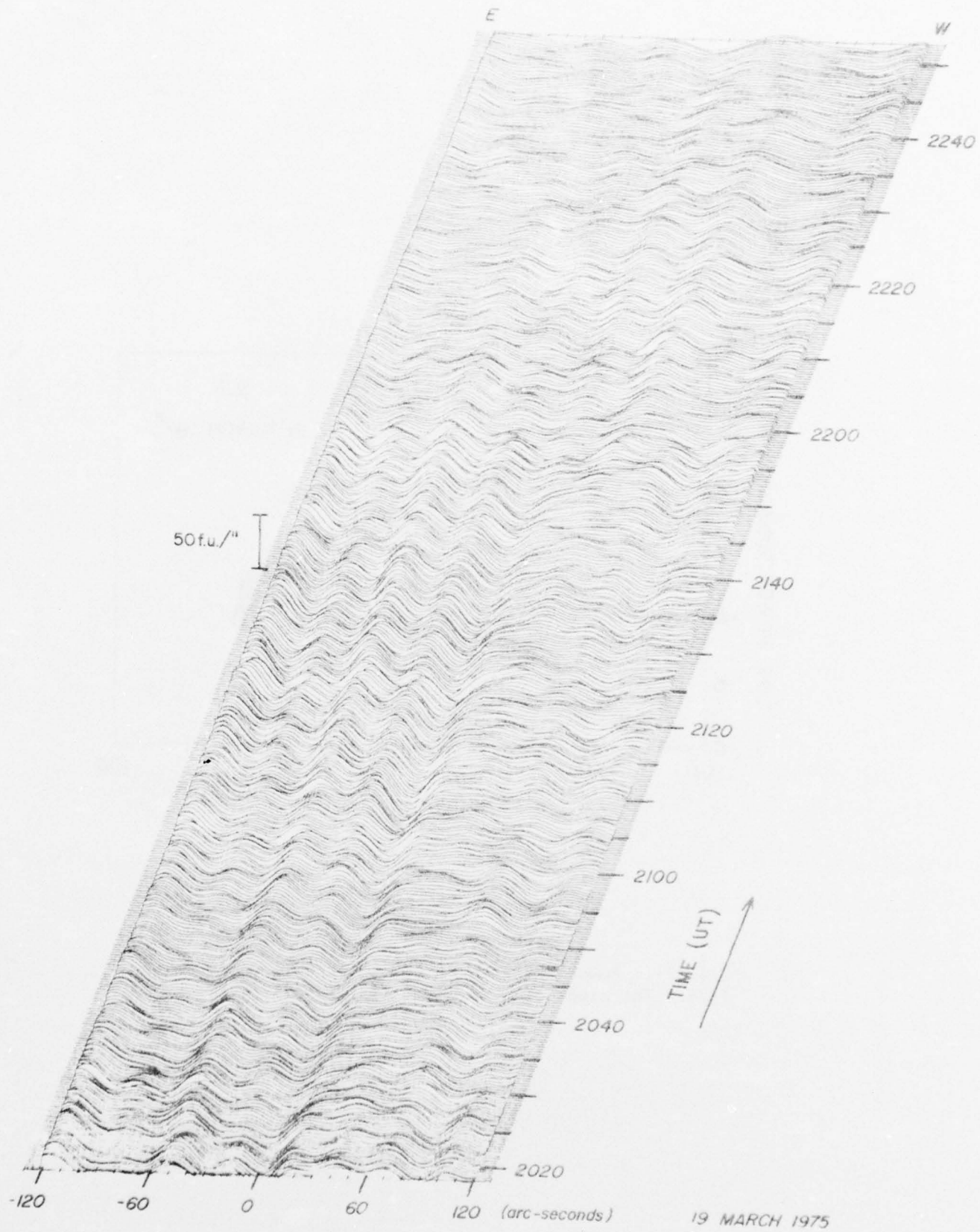


FIG. 10. Perspective plot of the center of the solar disk on 19 March 1975. 1 f.u. = $10^{-26} \text{ W m}^{-2} \text{ Hz}^{-1}$.

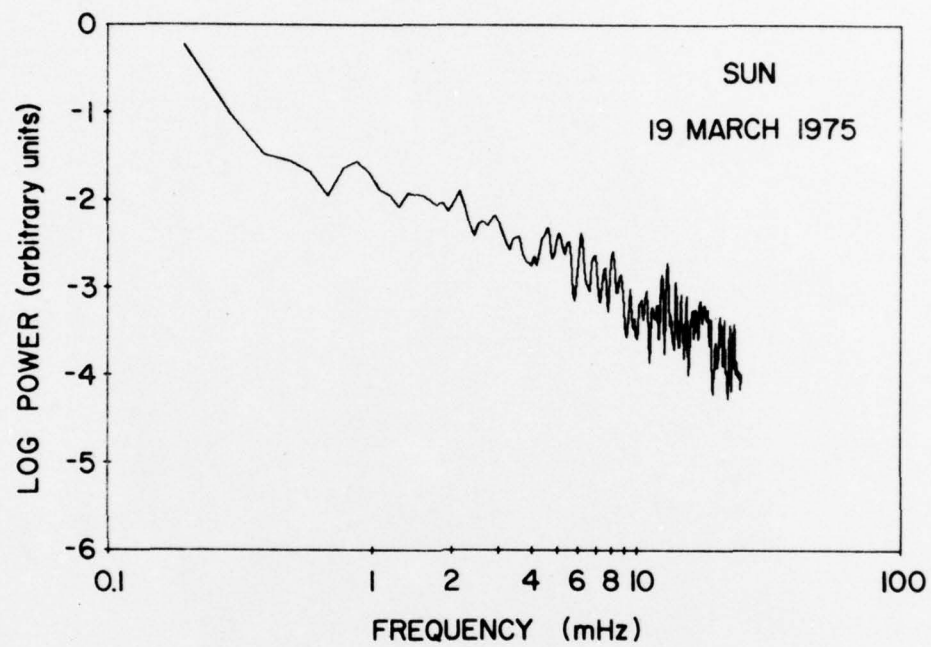


FIG. 11. Power spectrum of the solar data on 19 March 1975. The slope of a straight line fit is -1.6.

Lang [1974] using the Owens Valley interferometer at 3.7 cm observed periodic fluctuations of the quiet sun with periods of 180 to 750 seconds. The two-element interferometer strip chart recording presented by Lang looks similar to a single channel strip chart recording taken with the Stanford interferometer during the above observations. Kundu 1974b using the Hat Creek two-element interferometer at 1.3 cm found fluctuations in the complex visibility. These fluctuations lasted on the order of 4-7 minutes, but he was unable to find any periodicity. At Stanford we are so far unable to find any well-defined periodicity in the power spectra; however, the solar spectra have a slope of about -2. The sources of the observed emission have lifetimes longer than 2 hours; over a two-hour period the source structure changes very little. There are, however, fluctuations in these sources, and in a few cases new sources appeared during an observing run.

3. EQUATORIAL COORDINATES OF A SOURCE ON THE SUN

Over the last three decades the resolution of radio telescopes has improved dramatically. The first radio measurements of the sun were made with instruments whose beamwidth could be measured in degrees so that knowing the position of the sun to within arc-minutes was entirely satisfactory. As instrumental resolution was improved, individual features were resolved in the solar emission, and it became necessary to determine their location to within a number of arc-seconds. Radio telescopes now under construction, such as the Very Large Array, have potential resolutions of much less than one arc-second. To take full advantage of these increases in resolution, conversion from a solar

coordinate system to a topocentric system must be achieved with sub-arc-second accuracy.

Radio telescopes are typically pointed by specifying the source position in one of several coordinate systems. One of the most common sets uses the equatorial coordinates of right ascension and declination. For the sun, the right ascension and declination are continuously changing -- the right ascension by 240^s to 260^s per day and the declination by $\pm 1420''$ per day. This change of position requires that new right ascensions and declinations be computed frequently or that the instrument have the capability of tracking a source moving in its prime reference system.

The American Ephemeris and Nautical Almanac lists the position of the solar center for an observer at the center of the earth in several different coordinate systems. These listings are tabulated on a daily basis. For purposes of computing the apparent right ascension and declination of an arbitrary point on the sun, we have used the tabulated values of apparent right ascension, apparent declination, and true distance from the earth at 0 hours Ephemeris Time, and the solar P , B_o , and L_o angles at 0 hours Universal Time.

Apparent right ascension α_o and apparent declination δ_o give the position at which the solar center would appear for an observer at the center of the earth, including a correction for aberration. The right ascension is tabulated to 0.01^s and the declination to $0.1''$. The true distance from the earth R_d is the sun-to-earth center-to-center distance measured in astronomical units and is listed to 7 significant figures. These first three values may be interpolated to full accuracy using a second order interpolation. The solar P , B_o , and L_o angles are listed

in "The Ephemeris for Physical Observations" section. The P angle denotes the position angle of the northern extremity of the axis of rotation measured eastward from the north point of the disk. The P angle varies over $\pm 26.3^\circ$ in the course of a year. B_0 is the latitude of the apparent center of the sun as seen from the earth, and varies over $\pm 7.25^\circ$ during a year. The L_0 angle is the longitude of the apparent solar center as seen from the earth. The longitude is an arbitrary coordinate system which was placed on the solar surface and assumed to rotate at $13.2^\circ/\text{day}$. L_0 increases with time and completes one cycle in 27.3 days.

Since these six values are only tabulated on a daily basis, it is necessary to interpolate to find their magnitude at an arbitrary time. A Lagrange three-point interpolation was believed to be sufficiently accurate to represent the data. To test this hypothesis, the interpolation was performed on the right ascension and declination over a tabulated interval of two days to the days between and then compared to the true value at several times during the year. The results of this are shown in Table 2. In all cases the difference between the true values and the interpolated ones never exceeded 0.02^s in right ascension and $0.2''$ in declination. Since the tabulated interval used is really one day, the errors arising in practice will be considerably smaller.

As of January 1, 1974, Ephemeris Time was 44.5^s greater than UT1, the observed Universal Time corrected for polar motions, and was increasing by 1.1^s per year. When interpolating the apparent right ascension, declination, and true distance to the earth, this difference must be included. Each second of error in the estimation of the Ephemeris Time will result in an instrumental pointing error of 0.003^s in right ascension and a maximum error of $0.016''$ in declination.

There are a number of coordinate systems in use for listing the position of features on the sun. In one the latitude and Carrington longitude are given. This heliographic coordinate system rotates with the sun and most sources move relatively slowly with it. The heliocentric coordinate system gives the position in terms of the solar latitude and the distance in angle from the central meridian of the sun. The latter is sometimes referred to as the central meridian distance L_c , and may be found from the Carrington longitude L by

$$L_c = L_o - L \quad (5)$$

The Carrington meridians rotate as a rigid body but the sun does not. For most purposes it is better to use the central meridian distance of a source at a given time.

The nominal solar rotation rate at a latitude, B , is given by Allen (1964) as

$$13.39 - 2.7 \sin^2(B) \text{ degrees/day} \quad (6)$$

This formula was derived from observations of sunspots as they crossed the sun, and is probably not highly accurate for radio sources. However, it is the best estimate available, and it has been adopted at Stanford to compensate for the solar rotation during a day's observing session.

There are several ways to calculate the right ascension and declination of a solar source given the right ascension and declination of the solar center and the latitude and central meridian distance of the source. Woolard and Clemence (1966) show that for a feature having known distance Δ and position angle P_a from a given location, the new position may be written as

$$\begin{aligned}
\delta &= \delta_0 + \Delta \cos(P_a) \\
\alpha &= \alpha_0 + \Delta \sin(P_a) / \cos(\delta)
\end{aligned}
\tag{7}$$

assuming that terms on the order of $(\alpha - \alpha_0)^2$ and $(\delta - \delta_0)^3$ may be neglected. For a source the size of the sun these neglected terms may be as large as 5" near the limb. For a source at latitude B, a central meridian distance L_c , and a true distance from earth R_d , the source position may be written as

$$\begin{aligned}
\delta &= \delta_0 + \frac{959.63''}{R_d} [\cos(P) \cos(B_0) \sin(B) + \sin(P) \cos(B_0) \\
&\quad \cos(B) \sin(L_c) - \sin(B_0) \cos(B) \cos(L_c)] \\
\alpha &= \alpha_0 + \frac{63.975''}{R_d \cos(\delta)} [\sin(P) \sin(B) - \cos(P) \cos(B) \sin(L_c)]
\end{aligned}
\tag{8}$$

For most earlier radio telescopes these formulas provided sufficient accuracy for locating solar sources. With some of the newer instruments positions should be determined to better than 1", creating the need for a calculation with higher accuracy. To do this we compute the location of the source in three-dimensional space, and then convert this to apparent right ascension and declination.

Wollard and Clemence (1966) define equatorial rectangular coordinates as

$$\begin{aligned}
x &= R \cos(\delta) \cos(\alpha) \\
y &= R \cos(\delta) \sin(\alpha) \\
z &= R \sin(\delta)
\end{aligned}
\tag{9}$$

where R is the distance to the source.

We shall define a geocentric coordinate system in which the x' axis points from the center of the earth to the center of the sun, the z' axis

is in the plane defined by the earth's axis of rotation and the solar center and points approximately north, and the y' axis is the third member of a right-hand coordinate system. Transformation from the xyz coordinate system to the $x'y'z'$ system is given by

$$\begin{aligned}x' &= x \cos(\delta_0) \cos(\alpha_0) + y \cos(\delta_0) \sin(\alpha_0) + z \sin(\delta_0) \\y' &= -x \sin(\alpha_0) + y \cos(\alpha_0) \\z' &= -x \sin(\delta_0) \cos(\alpha_0) - y \sin(\delta_0) \sin(\alpha_0) + z \cos(\delta_0)\end{aligned}\tag{10}$$

Substituting equation (5) into equation (6) yields the position in rectangular coordinates in the $x'y'z'$ system

$$\begin{aligned}x' &= R[\cos(\delta) \cos(\delta_0) \cos(\alpha - \alpha_0) + \sin(\delta) \sin(\delta_0)] \\y' &= R[\cos(\delta) \sin(\alpha - \alpha_0)] \\z' &= R[\sin(\delta) \cos(\delta_0) - \cos(\delta) \sin(\delta_0) \cos(\alpha - \alpha_0)]\end{aligned}\tag{11}$$

Inversion of this transformation gives

$$\begin{aligned}\alpha &= \alpha_0 + \tan^{-1} \left[\frac{y'}{x' \cos(\delta_0) - z' \sin(\delta_0)} \right] \\ \delta &= \tan^{-1} \left[\frac{z' \cos(\delta_0) + x' \sin(\delta_0)}{\sqrt{y'^2 + \{x' \cos(\delta_0) - z' \sin(\delta_0)\}^2}} \right]\end{aligned}\tag{12}$$

Finally, we shall define a third coordinate system with its origin at the center of the sun such that

$$\begin{aligned}
x'' &= -R_s \cos(B) \cos(L_c) \\
y'' &= -R_s \cos(B) \sin(L_c) \\
z'' &= R_s \sin(B)
\end{aligned}
\tag{13}$$

where R_s is the radius of the sun. Allen (1964) gives a value for R_s of 0.0046523 astronomical units.

The transformation between the $x'y'z'$ coordinate system and the $x''y''z''$ system is written

$$\begin{aligned}
x' &= R_d + x'' \cos(B_o) + y'' \sin(B_o) \sin(P) - z'' \sin(B_o) \cos(P) \\
y' &= y'' \cos(P) + z'' \sin(P) \\
z' &= x'' \sin(B_o) - y'' \cos(B_o) \sin(P) + z'' \cos(B_o) \cos(P)
\end{aligned}
\tag{14}$$

In terms of a source latitude and central meridian distance, this becomes

$$\begin{aligned}
x' &= R_d - R_s [\cos(B_o) \cos(B) \cos(L_c) + \sin(B_o) \sin(P) \cos(B) \sin(L_c) \\
&\quad + \sin(B_o) \cos(P) \sin(B)] \\
y' &= R_s [\sin(P) \sin(B) - \cos(P) \cos(B) \sin(L_c)] \\
z' &= R_s [\cos(B_o) \cos(P) \sin(B) - \sin(B_o) \cos(B) \cos(L_c) \\
&\quad + \cos(B_o) \sin(P) \cos(B) \sin(L_c)]
\end{aligned}
\tag{15}$$

Substitution of these values for x' , y' , and z' in equation (12) yields the right ascension and declination of an arbitrary position on the solar surface for an observer at the center of the earth. This position doesn't include the effect of parallax due to the finite size of the earth. The Explanatory Supplement to the Ephemeris (1961) lists the formulas for finding

correct right ascension and declination when going from geocentric to topocentric coordinates as

$$\alpha = t_s - \tan^{-1} \left[\frac{\cos(\delta_g) \sin(t_s - \alpha_g)}{\cos(\delta_g) \cos(t_s - \alpha_g) - \rho \cos(\phi') \sin(\pi)} \right]$$

$$\delta = \tan^{-1} \left[\frac{\sin(\delta_g) - \rho \sin(\phi') \sin(\pi)}{\sqrt{\cos^2(\delta_g) + \rho^2 \cos^2(\phi') \sin^2(\pi) - 2 \cos(\delta_g) \sin(t_s - \alpha_g) \rho \cos(\phi') \sin(\pi)}} \right]$$

(16)

where t_s is the local sidereal time at the observatory, α_g and δ_g are the apparent right ascension and declination for an observer at the center of the earth, and π is the horizontal parallax. The values of $\rho \cos(\phi')$ and $\rho \sin(\phi')$ are tabulated for a number of observatories in The American Ephemeris and Nautical Almanac. For the observatory of the Stanford Radio Astronomy Institute, these values are

$$\rho \sin(\phi') = 0.60404$$

$$\rho \cos(\phi') = 0.79542$$

The magnitude of the horizontal parallax is often listed in addition to the source position in The American Ephemeris and Nautical Almanac. It may also be calculated given the distance of the source from the earth in astronomical units R_d by

$$\pi = \frac{8''.794}{R_d}$$

(17)

If the horizontal parallax is small, only the first order terms are necessary in the correction. The topocentric right ascension and declination may then be written as

$$\alpha = \alpha_g - \pi \left[\frac{\rho \cos(\phi') \sin(t_s - \alpha_g)}{\cos(\delta_g)} \right]$$

$$\delta = \delta_g - \pi \left[\rho \sin(\phi') \cos(\delta_g) - \rho \cos(\phi') \cos(t_s - \alpha_g) \sin(\delta_g) \right] \quad (18)$$

To convert from the solar latitude and central meridian distance to apparent right ascension and declination, the following procedure is followed.

1. Find the Ephemeris Time and UTI at the desired time for the calculation.
2. Use a second order interpolation for the apparent right ascension and declination of the solar center, the distance from the earth to the sun, and the solar P , B_o and L_o angles.
3. If solar longitude is given, convert from it to the central meridian distance using equation (5). If the central meridian distance is given, compensate for differential rotation using equation (6).
4. Compute the apparent right ascension and declination using equations (12) and (15).
5. Correct these apparent positions for parallax using equations (17) and (18).

Except where noted, the formulas contained within this section are exact. The accuracy of the answers is limited by the number of decimal

places to which the calculations are done. To achieve better than a 1% accuracy, the calculations must be done to at least seven significant figures.

4. MAXIMUM ENTROPY SOLUTIONS

Interferometers, such as the Stanford instrument, measure the Fourier transform of the source brightness distribution at a number of discrete points. The location of these points is determined by the antenna baseline as projected on the source brightness distribution. Each of these measurements is referred to as the complex visibility for that particular baseline. If all possible baselines of the complex visibility were available, we could in principle reconstruct the source brightness distribution exactly. In practice, interferometers must be of finite size, so that beyond a certain element spacing no measure of the complex visibility is obtained. Furthermore, baselines less than the maximum spacing are often left unmeasured because of instrumental limitations. This lack of data causes the reconstructed brightness distribution to be only an estimate of the true brightness distribution.

One of the more common methods of estimating the true brightness distribution is to assume that all unmeasured complex visibilities are zero. In one dimension this direct transformation may be written

$$b_0(x) = \sum_{i=1}^M a_i [V_i^{(R)} \cos(2\pi s_i x) - V_i^{(I)} \sin(2\pi s_i x)] \quad (19)$$

where M is the number of measurements, s_i is the interferometer element

spacing for the i^{th} measurement, and the complex visibility of the i^{th} measurement is $V_i = V_i^{(R)} + j V_i^{(I)}$, $j = \sqrt{-1}$. The weighting constant a_i may be used to taper the array's response in order to lower the sidelobe levels.

The direct reconstruction has several drawbacks. Except under special circumstances, the reconstructed brightness distribution will not agree exactly with the measurements, and furthermore, the magnitude of this discrepancy is independent of instrumental errors. In most cases this reconstruction will show regions with negative brightness temperatures, which are physically inadmissible. Finally, the sidelobe structure will be fairly complicated causing difficulty in the interpretation of the brightness distribution by those unfamiliar with the instrumental response. If tapering is used to decrease the sidelobe levels, the resolution of the instrument will be degraded significantly. Despite these disadvantages, the simplicity of this method has caused it to come into widespread use.

Another method which is computationally more complicated has come into use recently. It is often referred to as the maximum entropy method of reconstruction. We shall in the next few paragraphs summarize the method following the treatment of Wernecke and D'Addario (1976).

In reconstructing a brightness distribution, we wish to find a solution which is consistent with the measurements within the errors of these measurements. Unfortunately, for a finite number of measurements there are an uncountable number of solutions that can agree with them. It is necessary to select only one solution from this uncountable set. The solution should be physically admissible, which eliminates any solution containing a region of negative brightness. To select one solution from

those remaining in the set, we choose to use the solution which maximizes the entropy measure

$$H = \int \log [b(x)] dx \quad (20)$$

In one sense, the entropy may be thought of as a smoothness criterion. We find that this maximum entropy solution has two highly desirable characteristics: it is a solution that is physically admissible, and it agrees with the measurements within the measurement errors.

To perform the solution on a digital computer, we break the brightness distribution up into N equally spaced elements separated by a length of Δx . Each of these elements is referred to as a pixel. The entropy measure is then written discretely as

$$H = \Delta x \sum_{k=1}^N \log [b(x_k)] \quad (21)$$

We also define an error-squared term which describes the discrepancy between the reconstructed brightness distribution and the measurements as

$$E = \sum_{i=1}^M \frac{1}{\sigma_i^2} \left| v_i - \Delta x \sum_{k=1}^N b(x_k) \exp(j2\pi s_i x_k) \right|^2 \quad (22)$$

where σ_i^2 is the variance of the i^{th} measurement.

From these two terms we may then define an object function which we wish to maximize as

$$J(b(x_1), b(x_2), \dots, b(x_k)) = H - \lambda E \quad (23)$$

where λ is a Lagrange multiplier. Making λ larger tends to decrease the discrepancy between the estimated brightness distribution and the measurements.

There is no exact method for calculating λ so that the discrepancy between the reconstructed brightness distribution and the measurements is of a certain magnitude. Wernecke and D'Addario (1976) have shown that a reasonable estimate of λ may be made from

$$\lambda = \frac{\Delta x}{2(1 + V_1/\sigma_1)} \quad (24)$$

where V_1 is the visibility of the zero spacing and σ_1 is its variance. Further adjustment of λ may be necessary if this value doesn't give a satisfactory solution.

Differentiating the objective function J with respect to the ℓ^{th} pixel and setting this equal to zero, allows one to solve for the brightness of the ℓ^{th} pixel.

$$b(x_\ell) = \frac{D_\ell - \Delta x \sum_{k \neq \ell}^N P_{\ell,k} b(x_k) + \sqrt{[D_\ell - \Delta x \sum_{k \neq \ell}^N P_{\ell,k} b(x_k)]^2 + 4 \Delta x P_{\ell,\ell}}}{2 \Delta x P_{\ell,\ell}}$$

$$P_{\ell,k} = 2\lambda \sum_{i=1}^M \frac{1}{\sigma_i^2} \cos [2\pi s_i (x_\ell - x_k)] \quad (26)$$

$$D_\ell = 2\lambda \sum_{i=1}^M \frac{1}{\sigma_i^2} [V_i^{(R)} \cos(2\pi s_i x_\ell) - V_i^{(I)} \sin(2\pi s_i x_\ell)] \quad (27)$$

$P_{\ell,k}$ is the point source response for this particular set of measurements and D_ℓ is a representative of the direct transformation. The calculation is performed repetitively with ℓ varying from 1 thru N until the solution has satisfactorily converged to the maximum of the objective function. Since the maximum value of the objective function is unknown, there is no simple way to determine how far the solution is from convergence. A method which has performed adequately in practice is to continue iterating the solution until the reconstructed brightness changes insignificantly from one iteration to the next. In the maximum entropy

solutions which are in the next section, a change was considered to be insignificant if the pixels changed by an r.m.s. of less than 0.05%.

The point by point maximum entropy method has been implemented at Stanford on an IBM 370/168 computer. For a typical solar active region it was found that it takes about 100 iterations for a 55 pixel solution to converge satisfactorily. The approximate running time for each solution was less than 1 second, or a cost per solution for CPU time of under 20¢. While this is a considerably higher cost than finding the direct transform solution, the overall cost still comes out small when compared to the cost of obtaining the data and displaying the results.

Much of the data taken on the sun has included the polarized component of radiation from the sun. This data in general shows that the Stokes Q and U components are at or below the instrumental polarization levels. The Stokes V component within solar active regions may be significantly above the instrumental polarization. Ponsonby (1973) has derived an entropy measure for polarized radiation in terms of the Stokes parameters. Expressed discretely it is

$$H = \Delta x \sum_{k=1}^N \log [b_I^2(x_k) - b_Q^2(x_k) - b_U^2(x_k) - b_V^2(x_k)] \quad (28)$$

For the sun we can assume that the $b_Q(x)$ and $b_U(x)$ components are zero. This leaves

$$H = \Delta x \sum_{k=1}^N \log [b_I^2(x_k) - b_V^2(x_k)] \quad (29)$$

This equation is then decomposed into

$$H = \Delta x \sum_{k=1}^N \log [b_I(x_k) + b_V(x_k)] + \Delta x \sum_{k=1}^N \log [b_I(x_k) - b_V(x_k)] \quad (30)$$

Similarly if the complex visibilities are $V_I(s)$ and $V_V(s)$, the error-squared term is written as

$$E = \sum_{i=1}^M \frac{1}{\sigma_i^2} \left[\left| V_I(s_i) \Delta x \sum_{k=1}^N b_I(x_k) \exp(j2\pi s_i x_k) \right|^2 + \left| V_V(s_i) - \Delta x \sum_{k=1}^N b_V(x_k) \exp(j2\pi s_i x_k) \right|^2 \right] \quad (31)$$

which is equal to

$$E = \frac{1}{2} \sum_{i=1}^M \frac{1}{\sigma_i^2} \left\{ \left| [V_I(s_i) + V_V(s_i)] - \Delta x \sum_{k=1}^N [b_I(x_k) + b_V(x_k)] \exp(j2\pi s_i x_k) \right|^2 + \left| [V_I(s_i) - V_V(s_i)] - \Delta x \sum_{k=1}^N [b_I(x_k) - b_V(x_k)] \exp(j2\pi s_i x_k) \right|^2 \right\} \quad (32)$$

Breaking the entropy and error-squared terms into two parts such that subscript 1 terms are from the I+V components and the subscript 2 terms are from the I-V components, the object function may be written as

$$J = J_1 + J_2 = [H_1 - \lambda E_1] + [H_2 - \lambda E_2] \quad (33)$$

The J_1 and J_2 parts are solved separately for the I+V and I-V components of the radiation. The sum and difference of these two solutions is then taken to find $b_I(x)$ and $b_V(x)$. This was the method used

to solve for the polarized one-dimensional scans presented in the next section of this report.

5. DESCRIPTION OF SOLAR RADIO BURSTS

In this section we shall present the maximum entropy solutions for four radio bursts which have been observed with the Stanford interferometer. All of this data is presented as one-dimensional scans across the active region in approximately an East to West direction. The exact angle of the scans depends on the solar P angle, the declination, and hour-angle at the time of the observation. The scan angle in no case rotated in excess of 10° during any of these bursts. The reconstructed brightness distributions have an r.m.s. disagreement with the original complex visibility measurements of 5-15%. This disagreement is on the same order as the estimated instrumental measurement error of 10%. A listing of the bursts which have been observed is given below.

Date	Times of Observation (UT)	Interferometer Pointed At
7/ 3/73	1918 - 1941	N10 E22
9/ 2/73	2153 - 2253	S21 E55
10/ 6/74	2035 - 2256	N10 E70
6/16/76	2240 - 2408	N05 E50

With the exception of the 2 September 1973, the interferometer was pointed right at the location of the burst. The bursts of 6 October 1974 and 16 June 1976 were measured for both their total intensity and circularly polarized components of emission. Measurements of only the total intensity were obtained for the earlier two bursts.

The radio burst of 3 July 1973 was located at the site of a bright H α subflare. The maximum entropy solutions for this burst are shown in

Figures 12 thru 17. Before and after the burst the active region consisted of one predominant source and several lesser ones. A two-dimensional map made from observations of the interferometer for the entire day shows that the main source coincides in position with the primary sunspot of this active region. Figure 6 is a plot of the flux, position of the peak, and full-width to half-power of the predominant source versus time. There is a slight increase in the flux around 1926 UT, followed by two peaks at 1933 and 1936. The H α flare patrol film taken at the Sacramento Peak Observatory shows that the flare also had two distinct peaks, but earlier in time at 1931 and 1935. The flare itself brightened in a small region north and slightly west of the sunspot. Projecting the baseline of the Stanford interferometer on the sun at the time of the observation, we find that the flare would appear to the interferometer to be 5-10" west of the sunspot. At the times of maximum flux from the burst, the location of the peak radio brightness is 5" further west than before or after the burst. Furthermore, the width of the source is several arc-seconds wider during the times of maximum flux. Both of these effects would be expected to occur if the radio burst was emitting west of the sunspot radio emission, but at a distance not great enough to be resolved into two components. It appears in all likelihood that the burst emission is radiating from the same region as the solar flare, but with a several minute time delay.

The radio burst of 2 September 1973 had a lifetime in excess of one hour. Pre-burst scans, plotted in the first two frames, show three components. In the third frame, taken an hour later, all three of the components have increased dramatically in strength. The central component is strongest, and decays in brightness in the following frames. The left

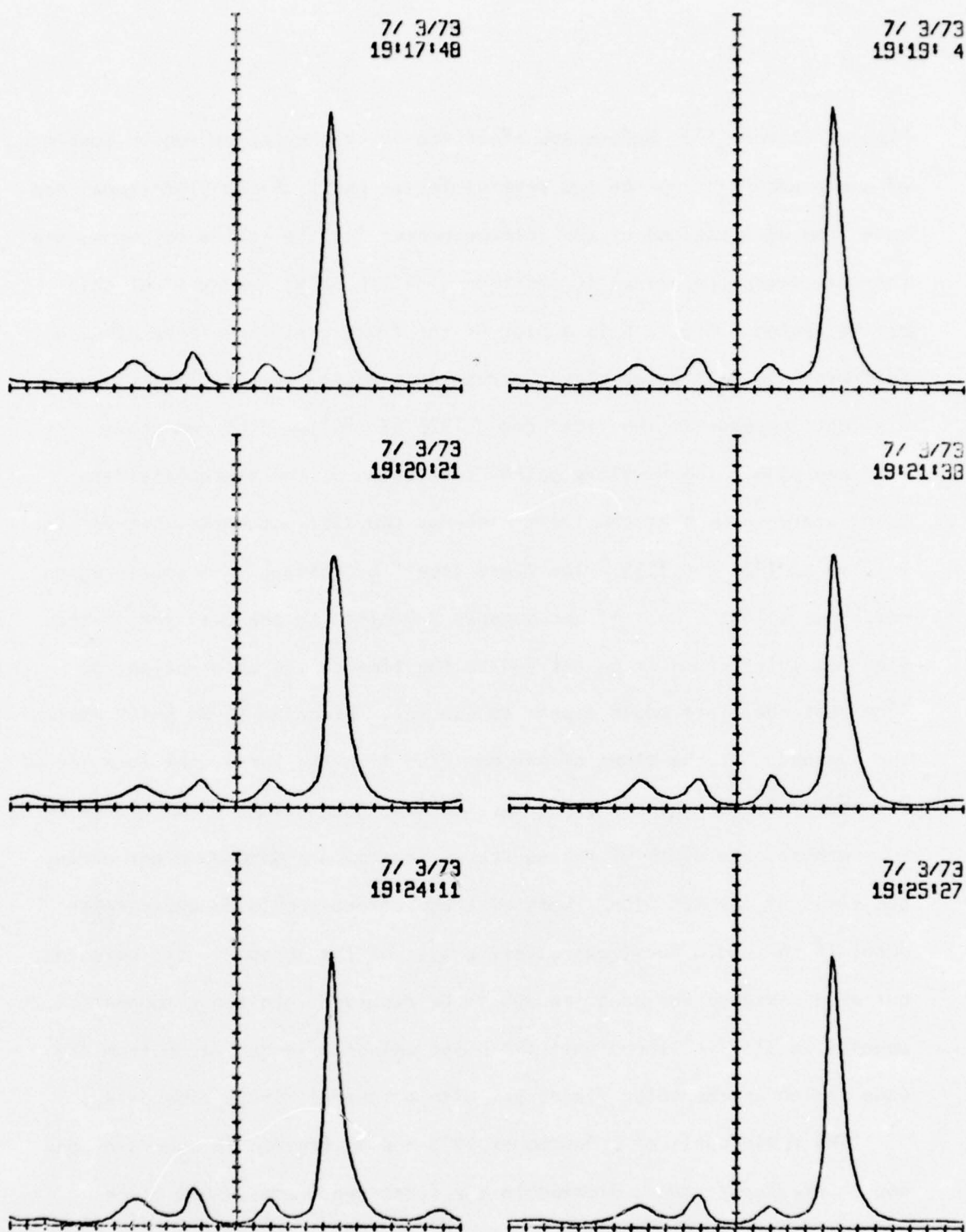


FIG. 12. Radio burst of 3 July 1973, frames 1 thru 6. Position is plotted along the abscissa, $10''$ per division. The ordinate shows the flux with a scale of $500 \text{ Jy}''$ per division. The solid line represents the brightness of the total intensity of the radiation. The time of each frame is given in UT.

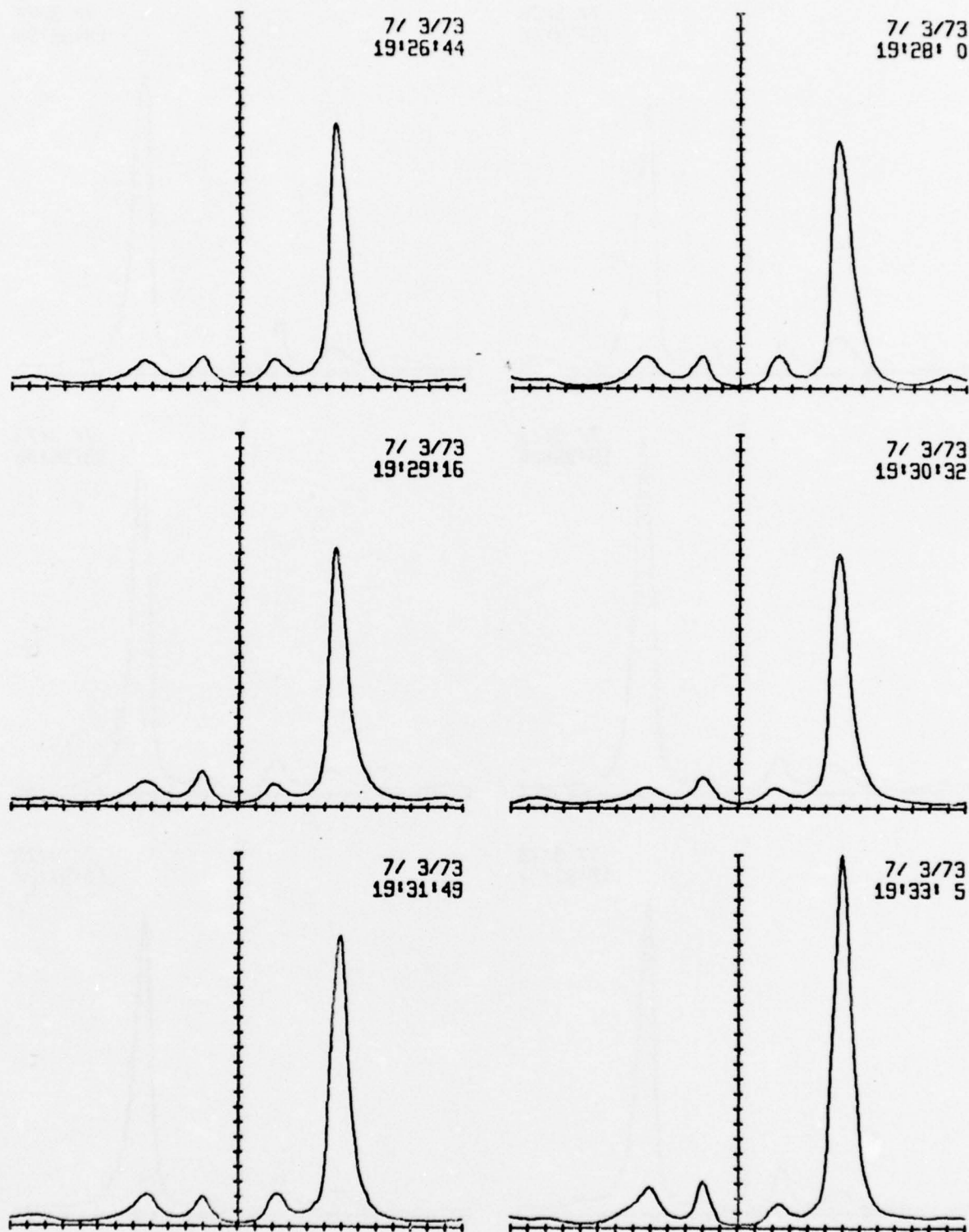


FIG. 13. Radio burst of 3 July 1973, frames 7 thru 12. Position is plotted along the abscissa, $10''$ per division. The ordinate shows the flux with a scale of $500 \text{ Jy}''$ per division. The solid line represents the brightness of the total intensity of the radiation. The time of each frame is given in UT.

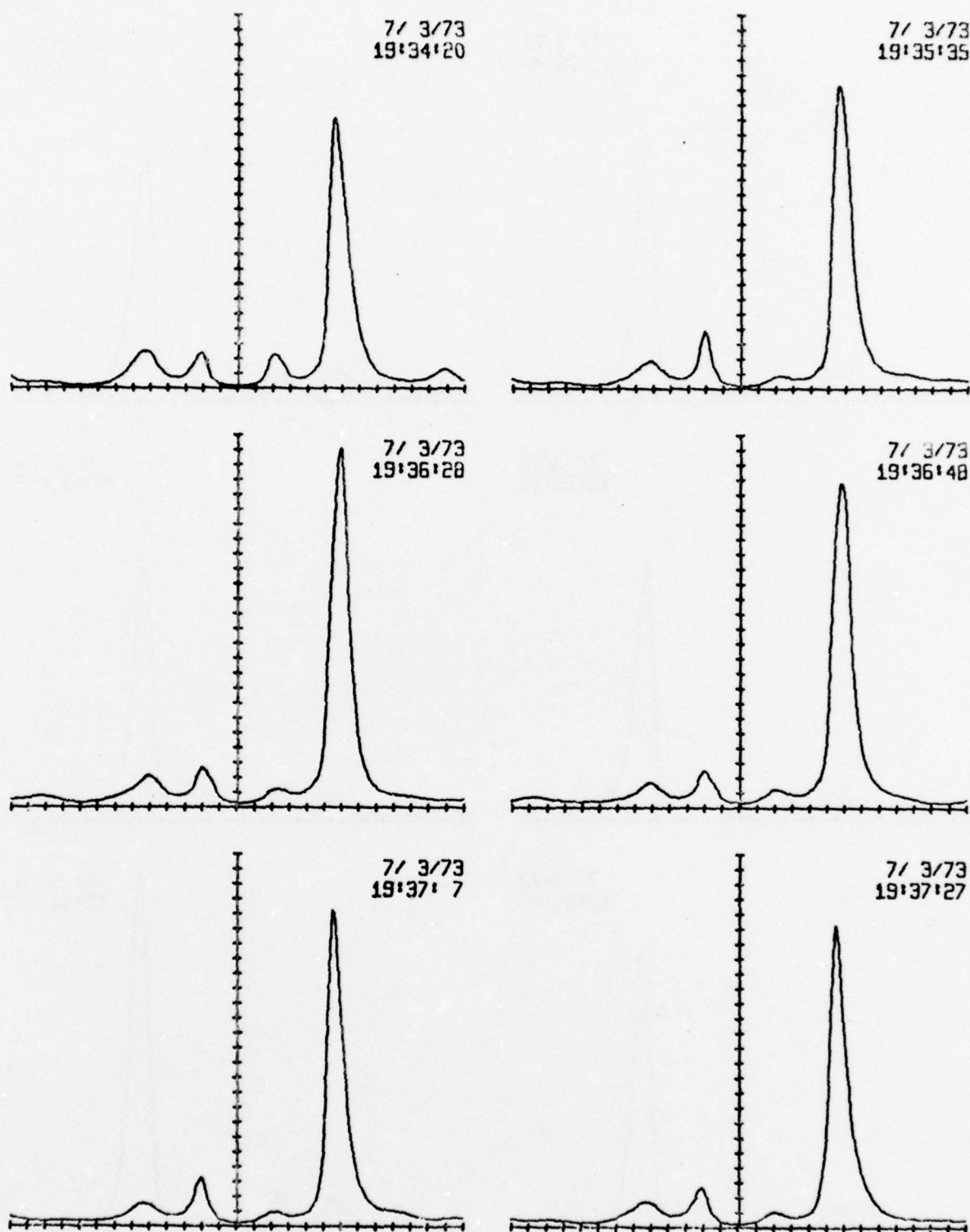


FIG. 14. Radio burst of 3 July 1973, frames 13 thru 18. Position is plotted along the abscissa, $10''$ per division. The ordinate shows the flux with a scale of $500 \text{ Jy}''$ per division. The solid line represents the brightness of the total intensity of the radiation. The time of each frame is given in UT.

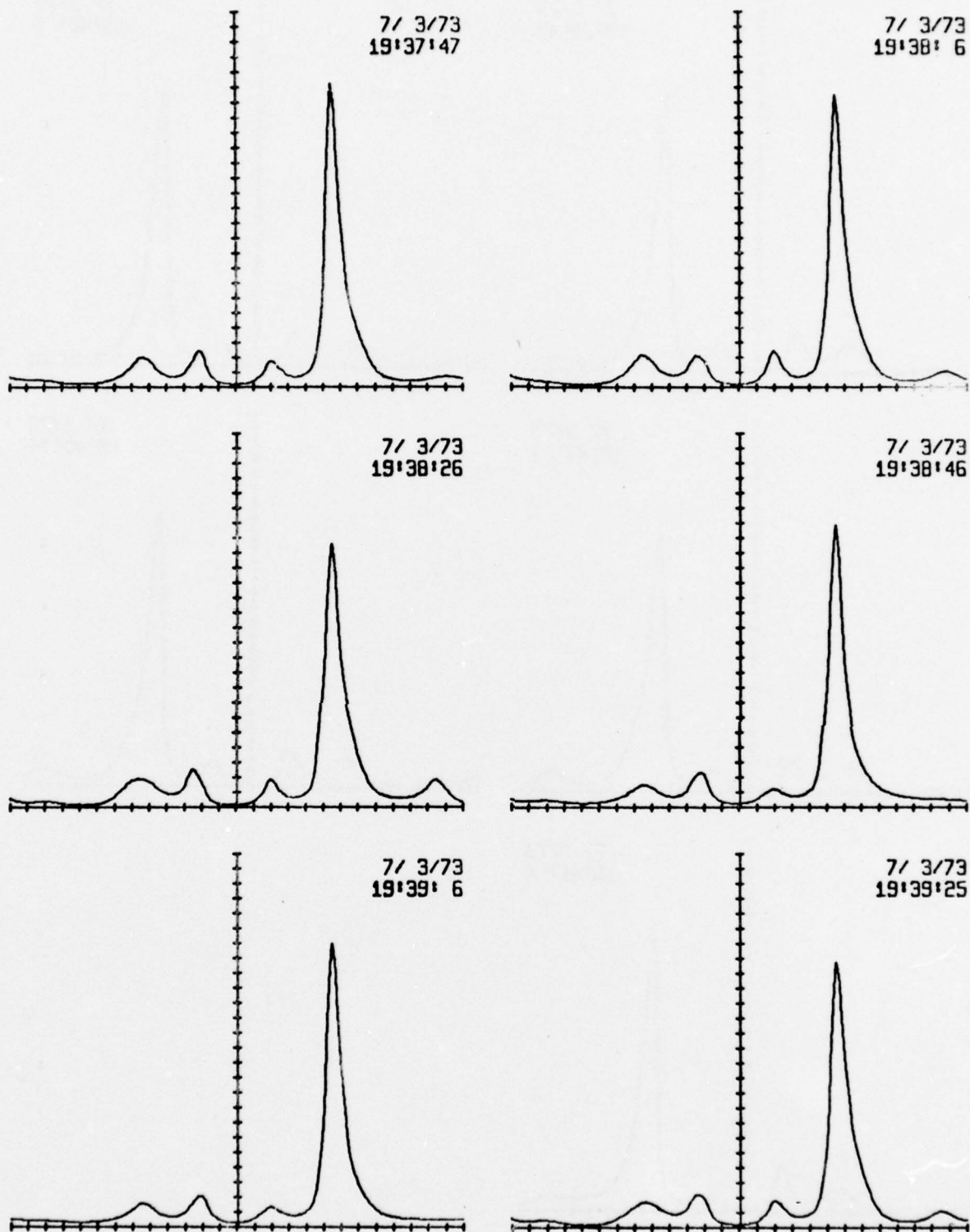


FIG. 15. Radio burst of 3 July 1973, frames 19 thru 24. Position is plotted along the abscissa, $10''$ per division. The ordinate shows the flux with a scale of $500 \text{ Jy}/''$ per division. The solid line represents the brightness of the total intensity of the radiation. The time of each frame is given in UT.

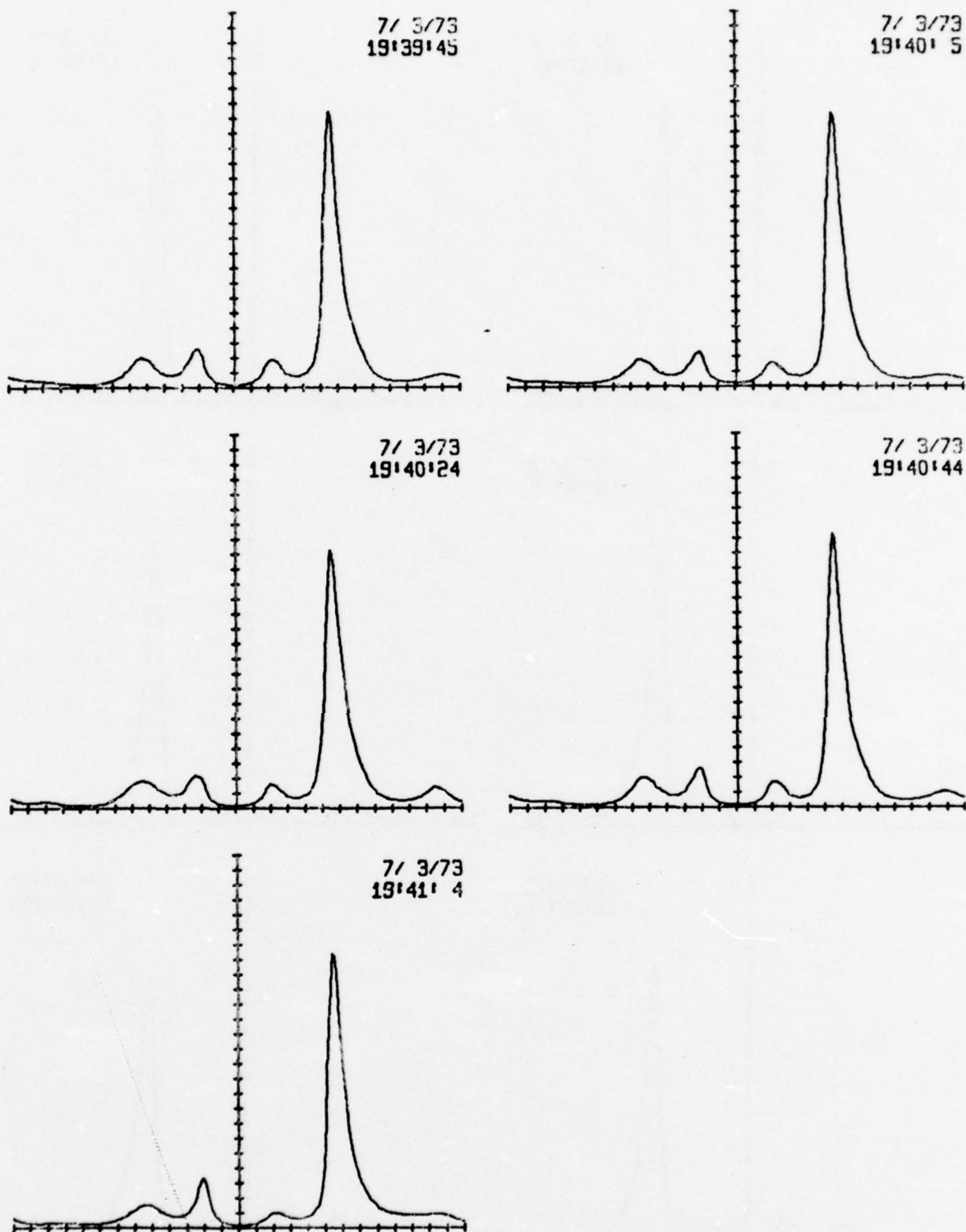


FIG. 16. Radio burst of 3 July 1973, frames 25 thru 29. Position is plotted along the abscissa, $10''$ per division. The ordinate shows the flux with a scale of $500 \text{ Jy}/''$ per division. The solid line represents the brightness of the total intensity of the radiation. The time of each frame is given in UT.

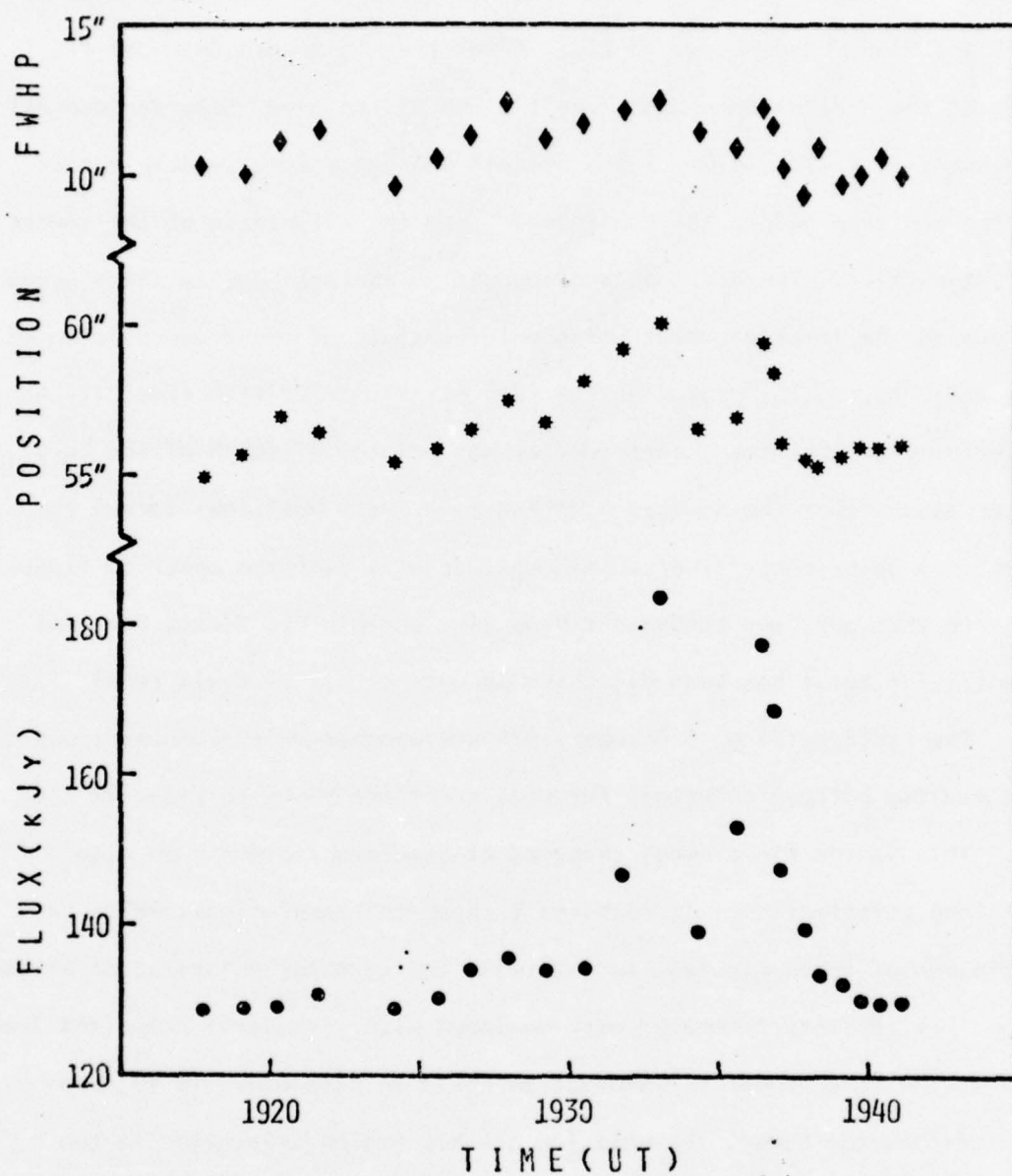


FIG. 17. Radio burst of 3 July 1973. Time in UT is plotted along the abscissa. The flux of the burst is plotted with circles. The relative position of the peak brightness is shown by the stars. The diamonds are the full-width of the source at the half-power point.

component increases in intensity until 2206 UT and then also begins to decay. The right component is only distinctly visible in the frames of 2154 and 2156. (See Figs. 18-21.) After that it merges into the right side of the central component. At the end of the event only the central component is still visible. The overall source is considerably broader at the end than before the event began, and the brightness of the source is intensified. The drift of the sources to the left during these scans is due to the interferometer being pointed south of the true position of the radio burst. By measuring the rate of this drift with time, it can be determined that the interferometer was pointed 4' south of the burst, if we assume that the sources didn't change their positions during the event. A pointing error of this magnitude will decrease observed fluxes by more than 50%, and consequently we give no absolute fluxes for this event. The burst has been discussed in more detail by Felli et al. (1975).

The radio burst of 6 October 1974 was another multi-component event. The maximum entropy solutions for this event are shown in Figs. 22 thru 24. This is the first burst observed at Stanford for which we also obtained polarization. It requires 6 separate integrations, which take a minimum of three minutes, to determine the circular polarization of one scan. If the interferometer were equipped with circularly polarized feed-horns, the same amount of information could be determined in 40 seconds.

Before the burst, the emission of this region originated in two components. The left component had a flux of 57 kJy and was right-hand polarized at 5%. This is not significant considering the estimated instrumental polarization levels. The right component had a flux of 56 kJy and was right-hand polarized at 14%. For purposes of computing the flux

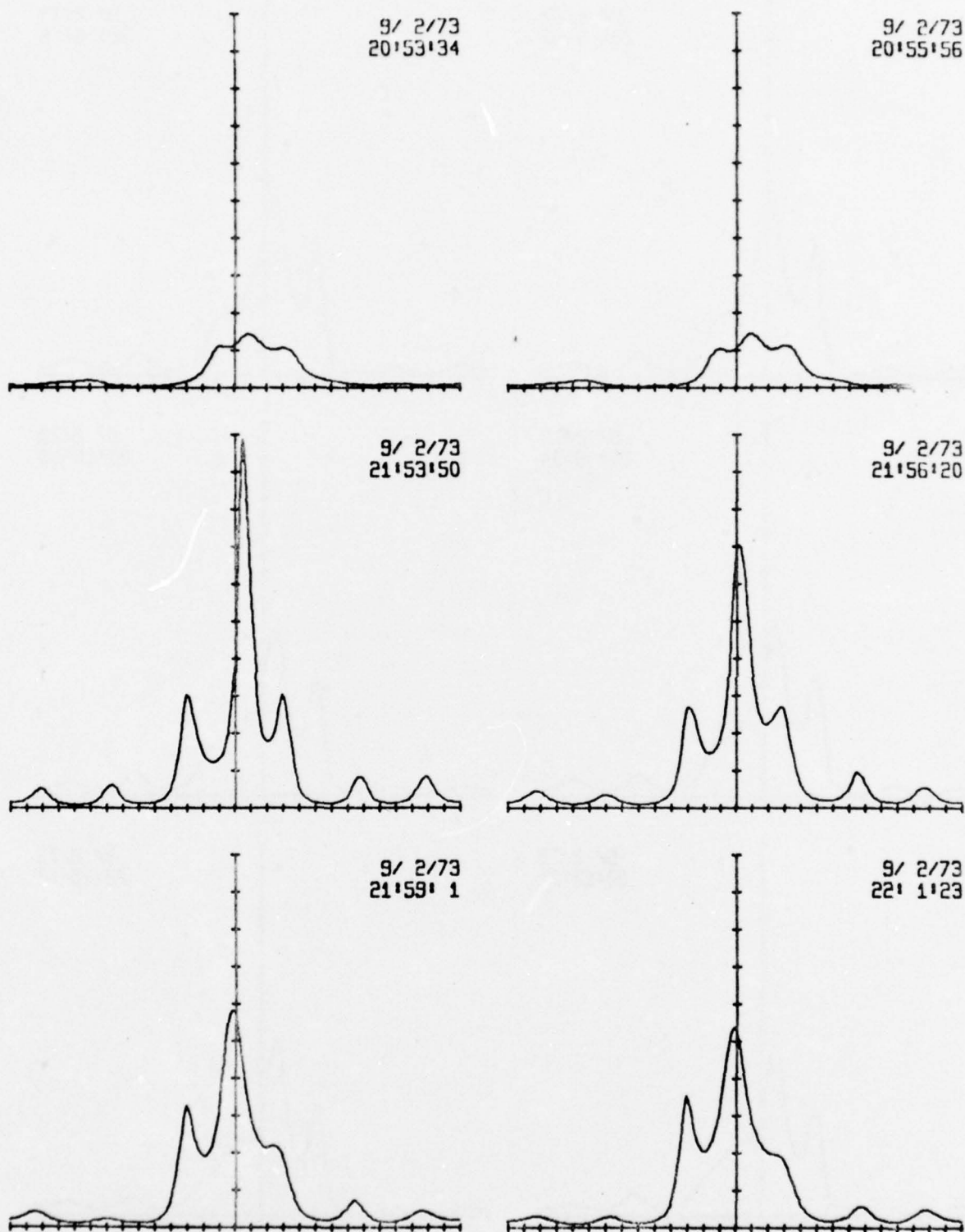


FIG. 18. Radio burst of 2 September 1973, frames 1 thru 6. Position is plotted along the abscissa, 10" per division. The ordinate shows flux with an unknown, but constant, scaling factor. The solid line represents the brightness of the total intensity of the radiation. The time of each frame is given in UT.

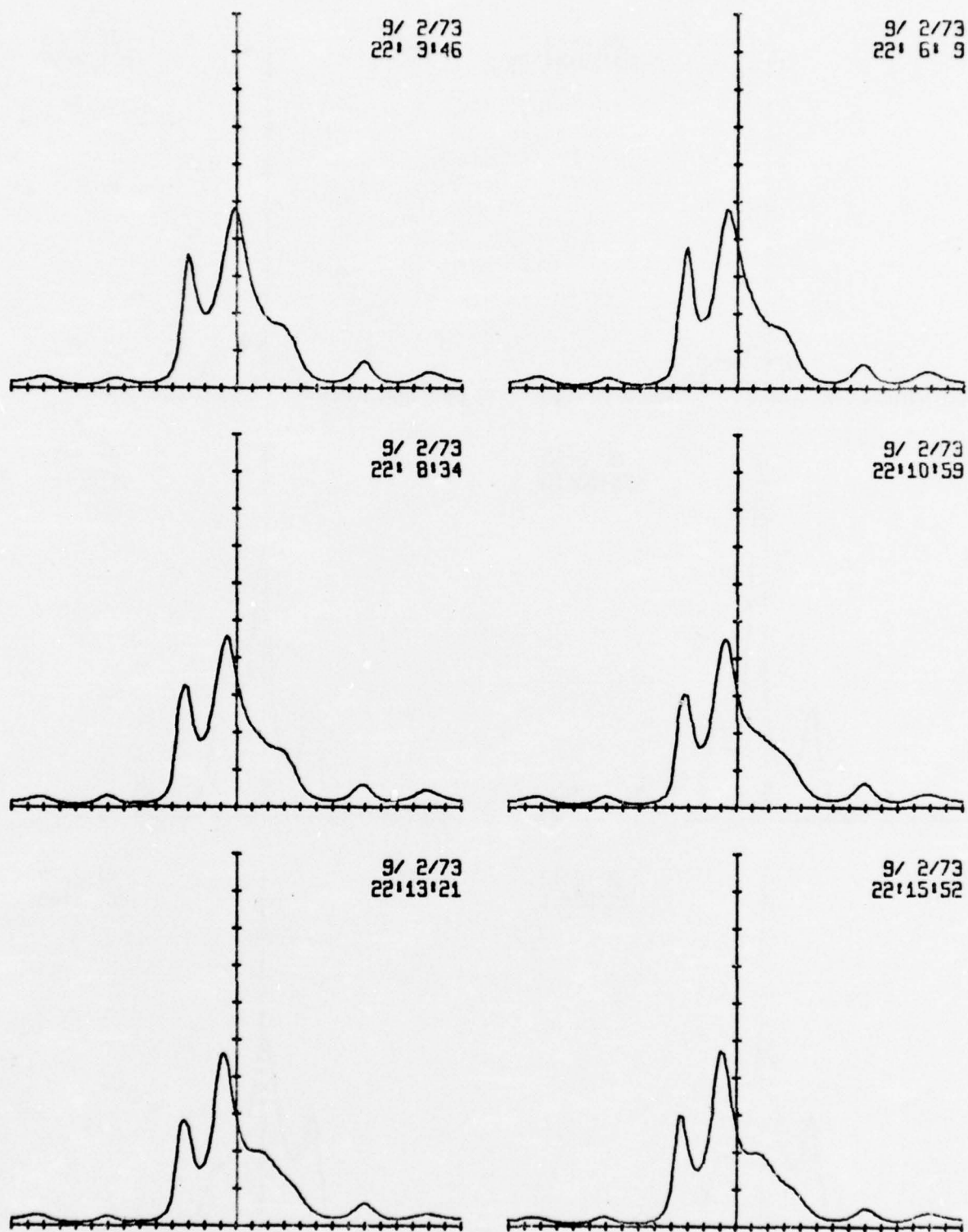


FIG. 19. Radio burst of 2 September 1973, frames 7 thru 12. Position is plotted along the abscissa, 10'' per division. The ordinate shows flux with an unknown, but constant, scaling factor. The solid line represents the brightness of the total intensity of the radiation. The time of each frame is given in UT.

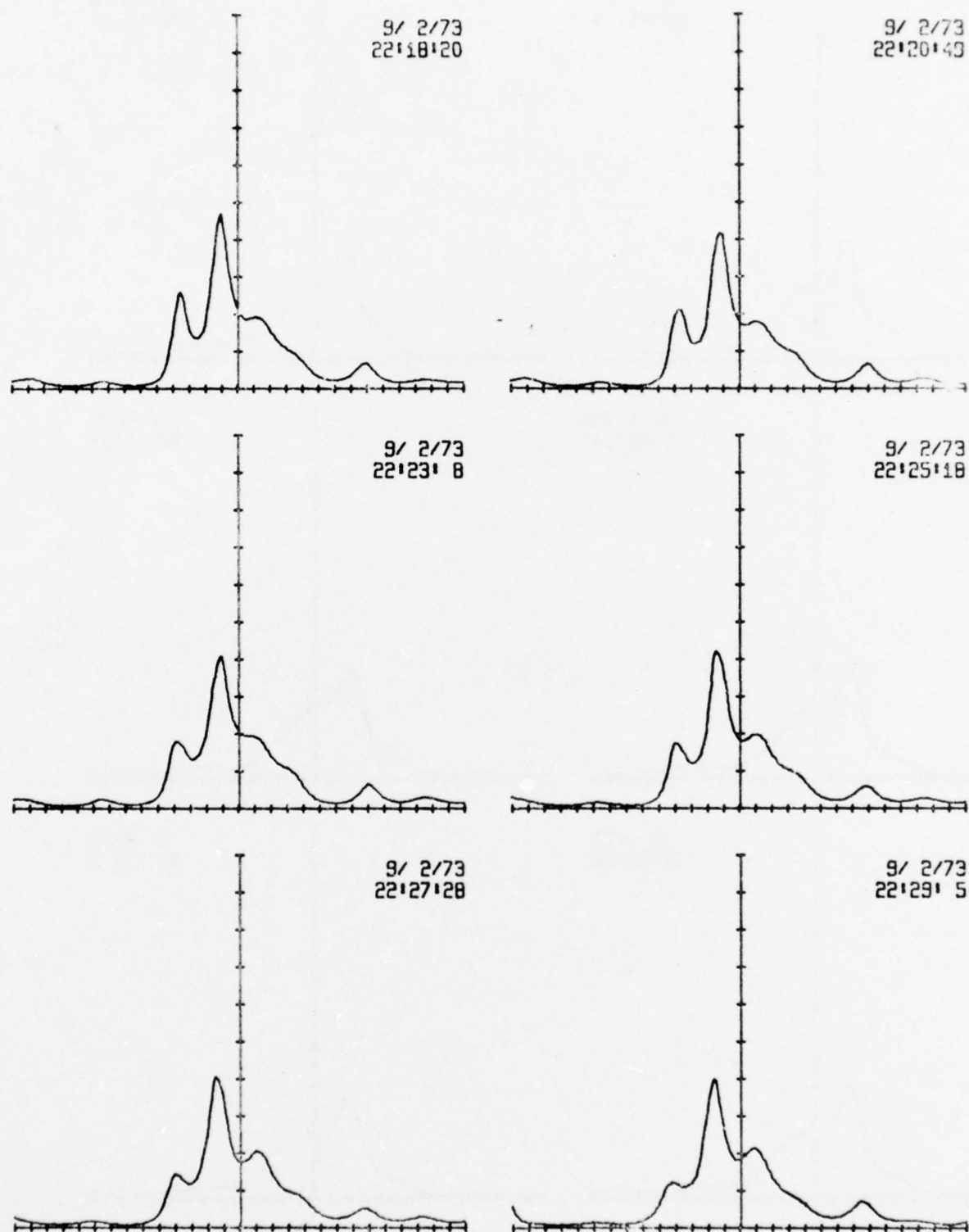


FIG. 20. Radio burst of 2 September 1973, frames 13 thru 18. Position is plotted along the abscissa, $10''$ per division. The ordinate shows flux with an unknown, but constant, scaling factor. The solid line represents the brightness of the total intensity of the radiation. The time of each frame is given in UT.

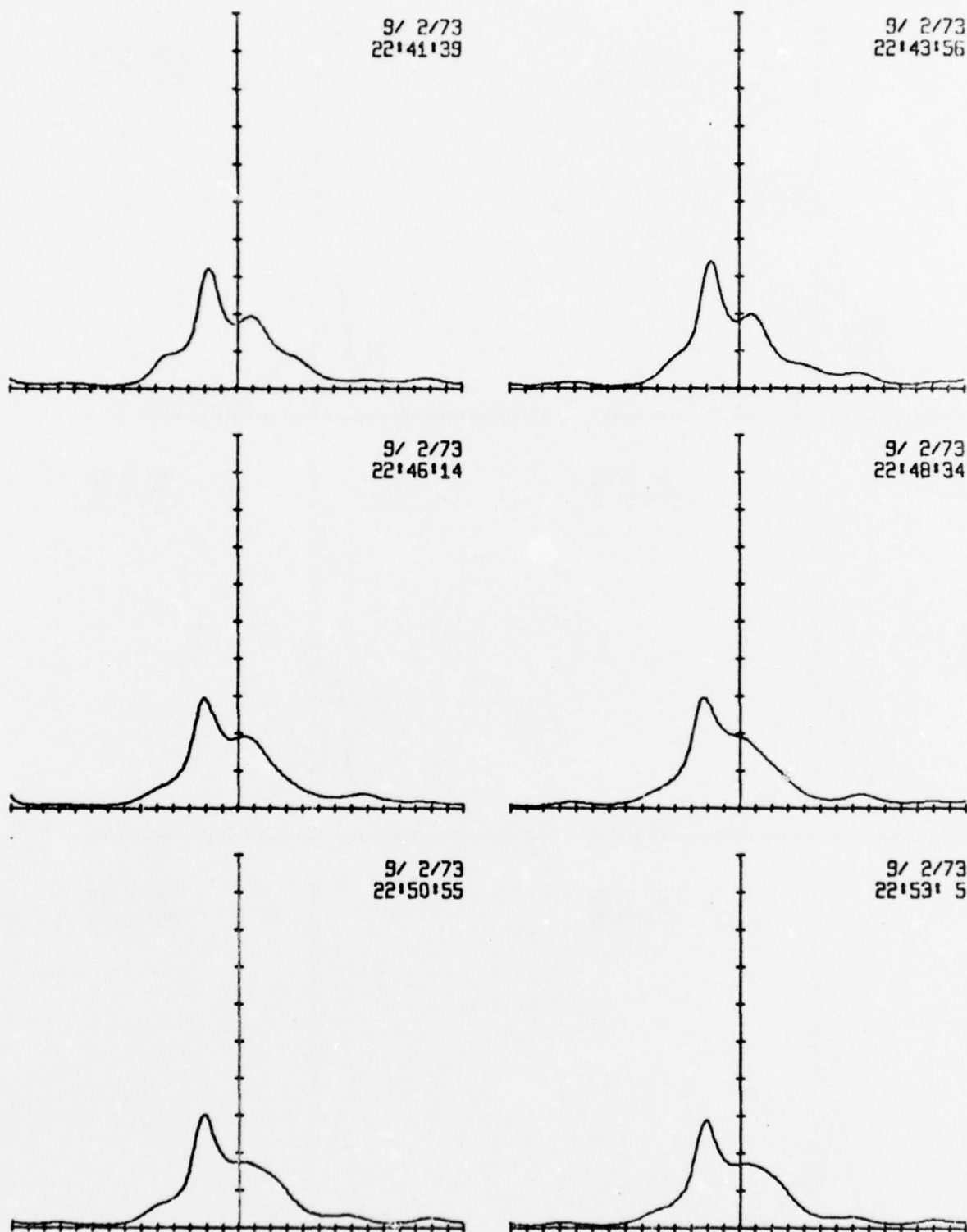


FIG. 21. Radio burst of 2 September 1973, frames 19 thru 24. Position is plotted along the abscissa, 10" per division. The ordinate shows flux with an unknown, but constant, scaling factor. The solid line represents the brightness of the total intensity of the radiation. The time of each frame is given in UT.

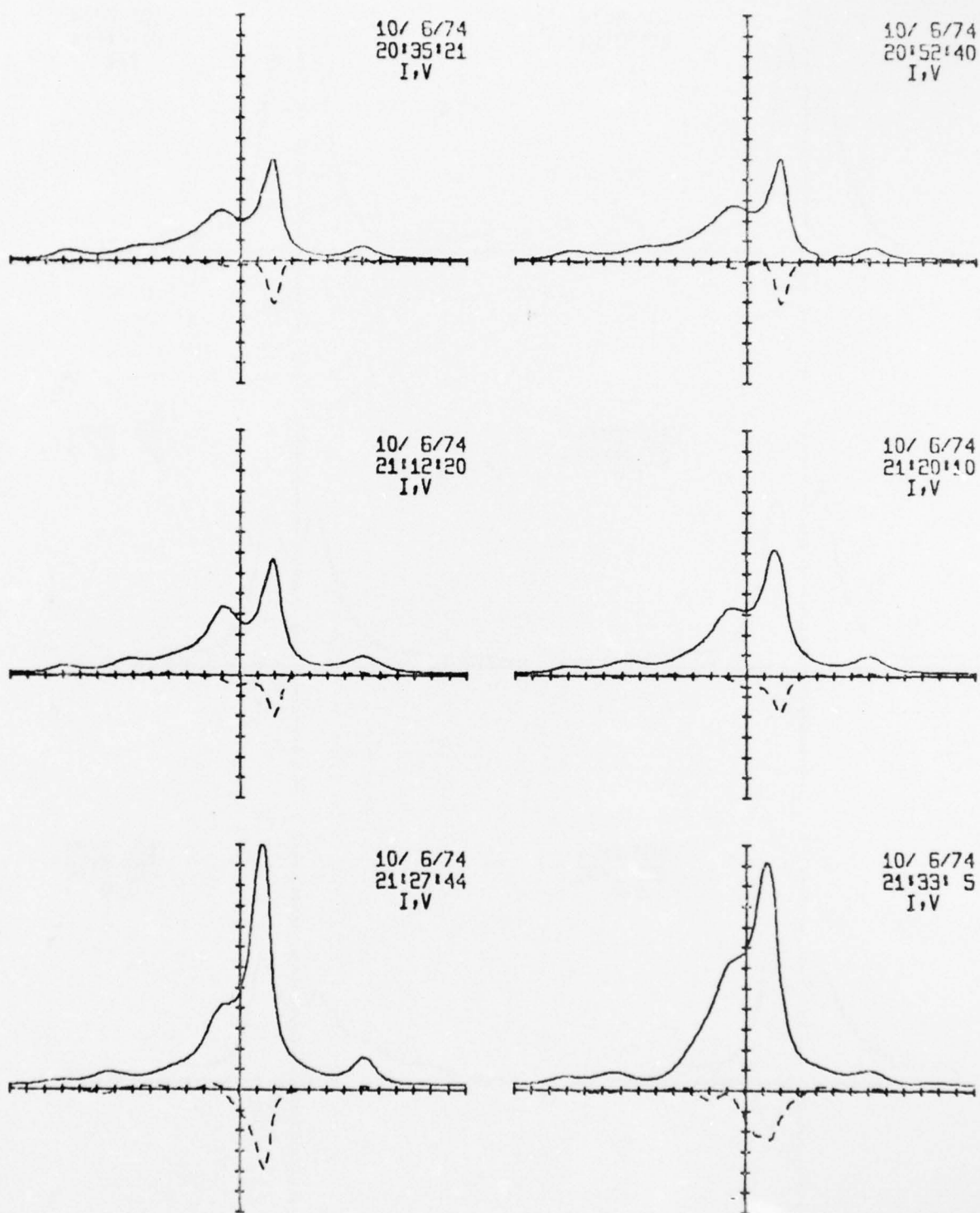


FIG. 22. Radio burst of 6 October 1974, frames 1 thru 6. Position is plotted along the abscissa, 10'' per division. The ordinate shows the flux with a scale of 500 Jy/'' per division. The solid line represents the brightness of the Stokes I component, the dashed line the Stokes V component. Time of each frame is given in UT.

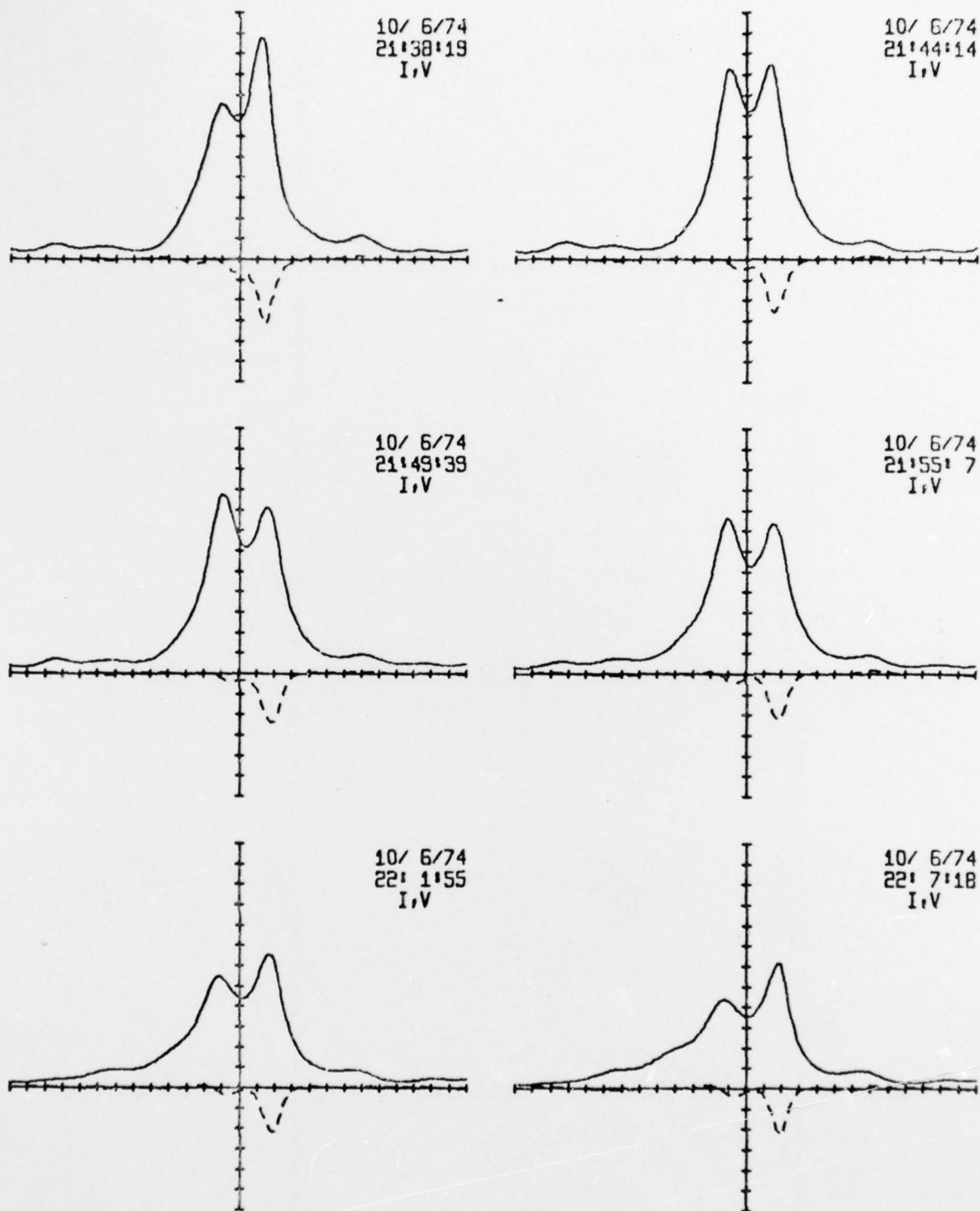


FIG. 23. Radio burst of 6 October 1974, frames 7 thru 12. Position is plotted along the abscissa, 10'' per division. The ordinate shows the flux with a scale of 500 Jy/'' per division. The solid line represents the brightness of the Stokes I component, the dashed line the Stokes V component. The time of each frame is given in UT.

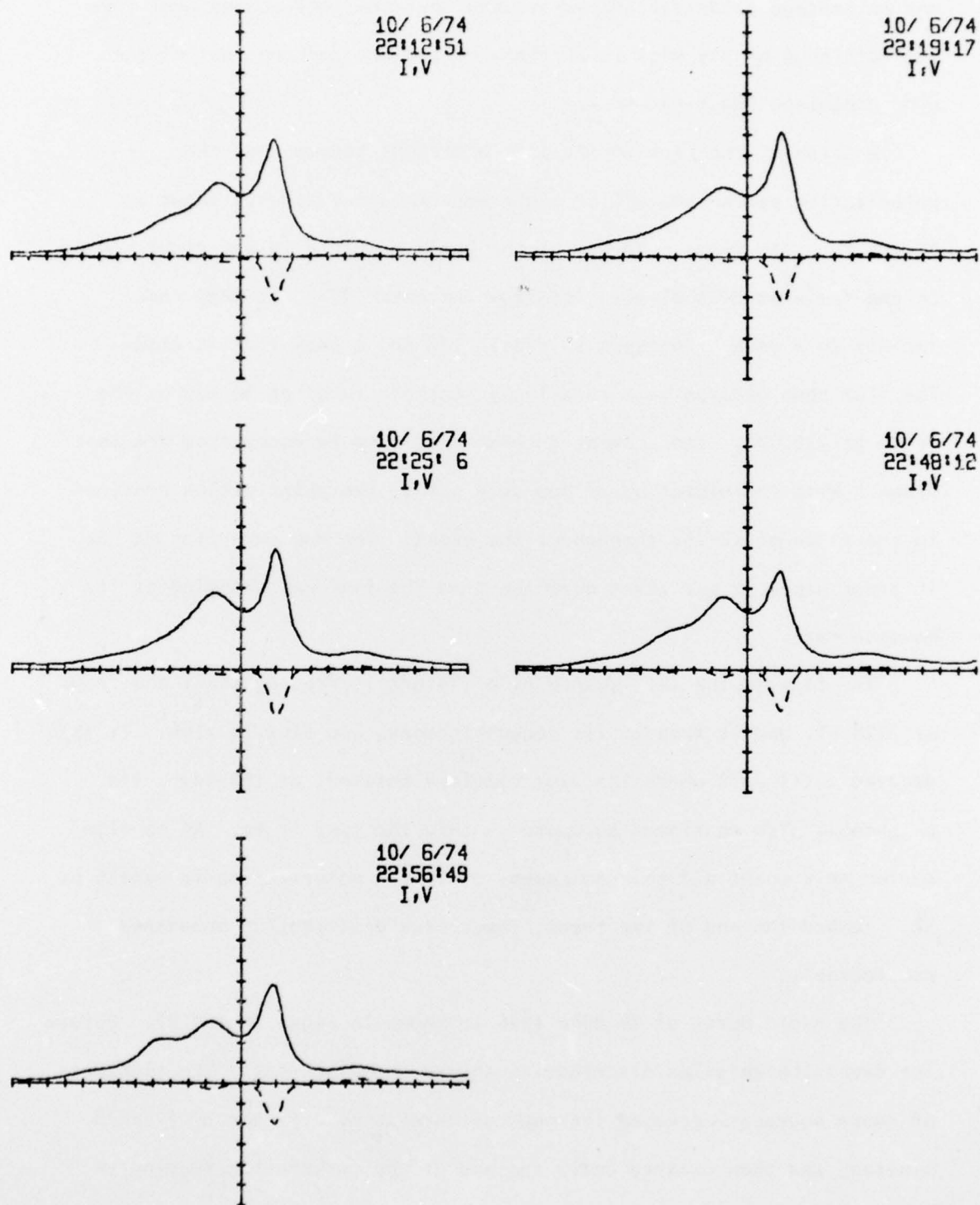


FIG. 24. Radio burst of 6 October 1974, frames 13 thru 17. Position is plotted along the abscissa, 10" per division. The ordinate shows the flux with a scale of 500 Jy/" per division. The solid line represents the brightness of the Stokes I component, the dashed line the Stokes V component. The time of each frame is given in UT.

and percentage polarization, we assumed that the left source went from the left edge of the plot to 2" right of center, and the rest of the plot contained the right source.

A graph of the flux in the left and right sources and the polarization percentage of the right source versus time is shown in Figure 25. The first evidence of the burst occurred in the right source in the frame at 2115 UT when its flux increased 20%. It then rose rapidly to a peak brightness in frame 2128 and a peak flux in 2138. The flux then decayed to a relatively constant level of 90 kJy by the frame at 2207 UT. The peak brightness continued to decay thru the last frame. With the exception of one data point, the polarization remained in the range of 12-15% throughout the event. The one exception may be in error since it was taken near the time the flux was changing at its maximum rate.

The flux of the left source didn't start increasing until the frame at 2128 UT, and it rose to its peak brightness and flux in 2144. It then decayed until 2212 where its flux remained constant at 100 kJy. Its brightness also continued to decrease thru the last frame. At no time during this event did this component exhibit a polarization in excess of 5%. Toward the end of the event, the source distribution broadened considerably.

The radio burst of 16 June 1976 is shown in Figs. 26 and 27. Before the event the emission distribution showed three sources. The rightmost of these sources increased its peak brightness by a factor of 7 in 15 minutes, and then decayed until the end of the observation 40 minutes later. The other two components showed much smaller increases in their

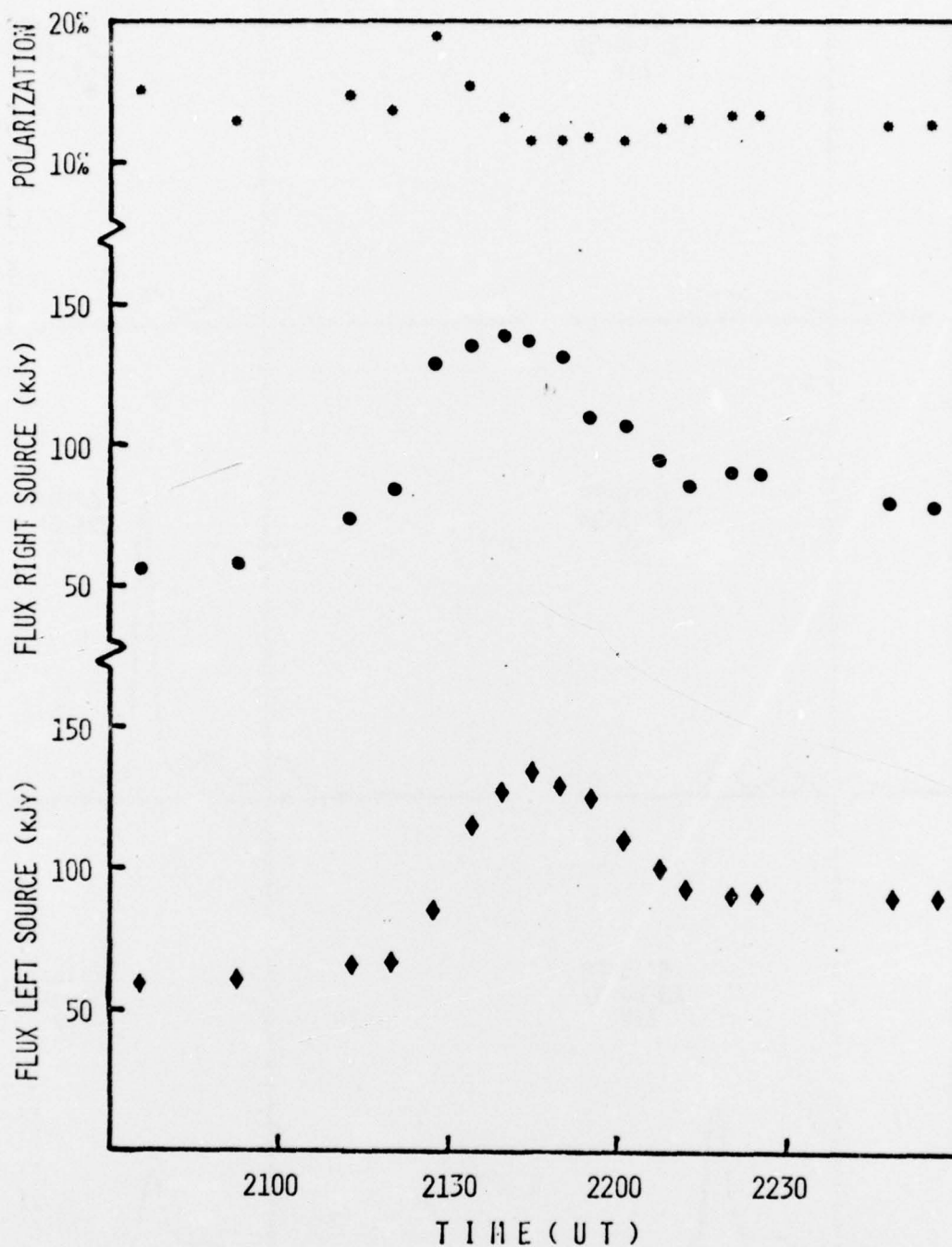


FIG. 25. The two component radio burst of 6 October 1974. The time in UT is plotted along the abscissa. The diamonds show the flux of the left component, and the circles the flux of the right component. The percentage of right circular polarization of the right source is shown by the stars. The left source had no significant polarization.

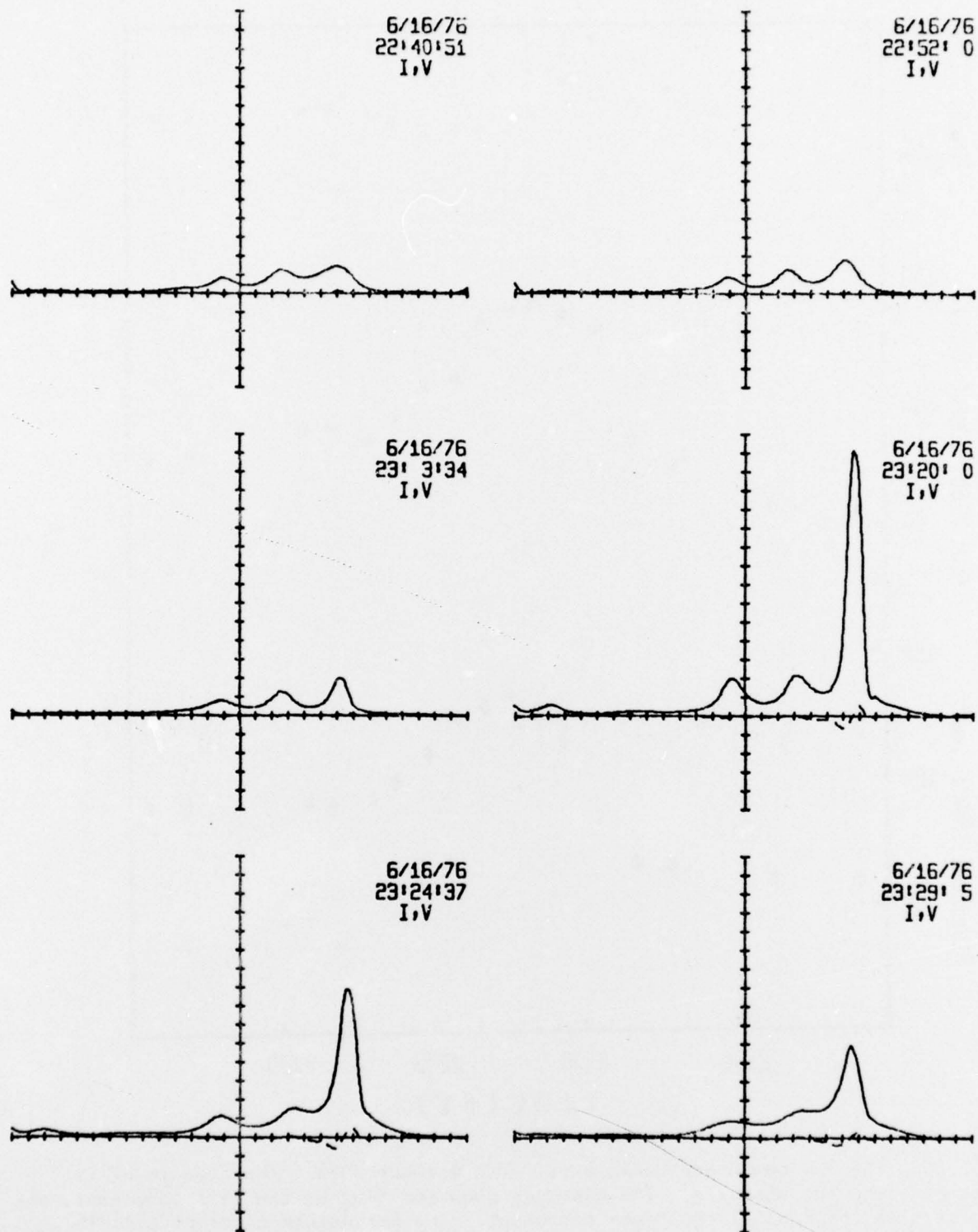


FIG. 26. Radio burst of 16 June 1976, frames 1 thru 6. Position is plotted along the abscissa, 10" per division. The ordinate shows the flux with a scale of 500 Jy/" per division. The solid line represents the brightness of the Stokes I component, the dashed line the Stokes V component. The time of each frame is in UT.

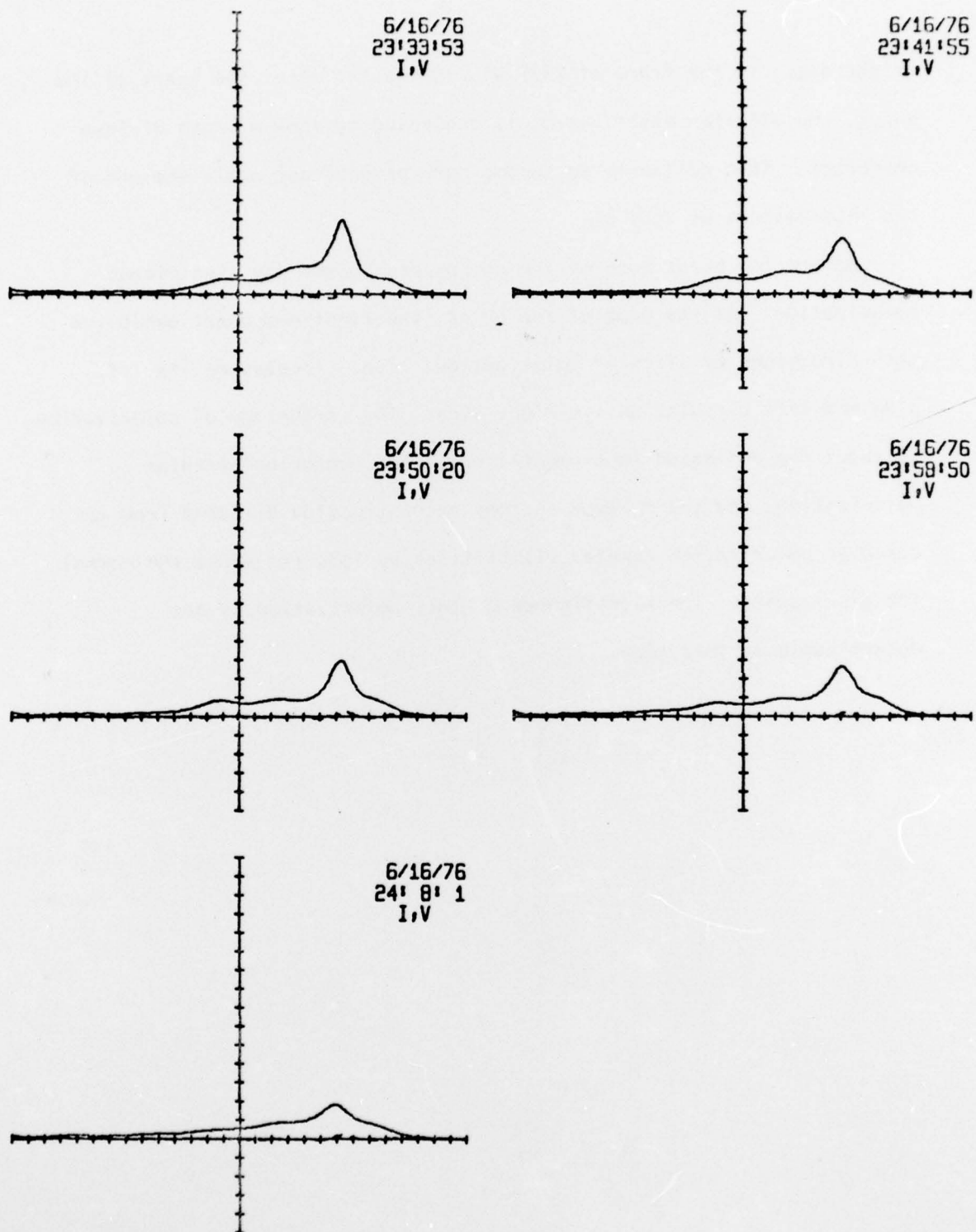


FIG. 27. Radio burst of 16 June 1976, frames 7 thru 11. Position is plotted along the abscissa, 10'' per division. The ordinate shows flux with a scale of 500 Jy/'' per division. The solid line represents the brightness of the Stokes I component, the dashed line the Stokes V component. The time of each frame is in UT.

brightness. In the frame of 2329 UT, 10 minutes after the start of the burst, the emission distribution is beginning to show a broad diffuse character. This continues to become more predominant until the end of the observations at 2408 UT.

Before the burst none of the components showed any significant polarization. At the peak of the burst, the right component exhibited both directions of circular polarization, right circular on its left side and left circular on its right side. The percentage of polarization is about the estimated instrumental error for measuring circular polarization, and the maximum entropy reconstruction differed from the circular polarization complex visibilities by 25%, far above the normal 10% discrepancy. The significance of this polarization is not determinable at this time.

6. INTERPRETATION OF THE RADIO BURSTS

Kundu (1965) has classified microwave radio bursts into three types, each of which is thought to be caused by a distinct emission process. A simple burst (Type A) is characterized by a rapid rise to a peak value and a subsequent slower decline. Its duration is on the order of 1 to 5 minutes. The burst may be partially circularly polarized, and its diameter is generally in the range of $1'$ to $1.6'$. The burst is caused by the emission of non-thermal bremsstrahlung or synchrotron radiation from the energetic electrons released and accelerated during a flare.

The post-burst emission (Type B) follows a simple burst or a group of simple bursts. Its duration is several minutes to several hours and its polarization is of the same nature as the simple burst which preceded it. The source of the emission appears to radiate from a diffuse regions of relatively large diameter ($>3'$). This type of burst appears to be caused by thermal bremsstrahlung.

The gradual rise and fall burst (Type C) is characterized by a slow rise to a maximum intensity and a comparatively slower decline to the pre-burst level. Its duration is on the order of 10 minutes or longer. In most cases the emission is partially circularly polarized. The source of the emission is a localized hot region of small diameter ($<1'$). This type of burst represents the preheating and compression of the flare region. Kundu (1965) believes that most solar microwave radio bursts may be represented by one or more of these three classifications.

The event of 3 July 1973 was a simple burst. The burst was coincident in time and position with an $H\alpha$ subflare. However, the two peaks in the radio brightness were 1-2 minutes later than the corresponding two peaks in the $H\alpha$ light curve. The delay implies that the electrons

accelerated in the flare process took several minutes to travel to a region in which their microwave radiation could propagate away from the sun. The diameter of both the radio burst and the subflare was less than 15". The location of the radio emission from the radio burst is not the same as the emission from the S-component. Figure 17 shows the burst emission to be approximately 5" west of the S-component emission. This is consistent with the S-component emission arising above the sunspot and the burst emission originating above the subflare region.

The other three radio events observed at Stanford were all post-bursts. In each case the time resolution of the interferometer was insufficient to resolve the simple burst which most likely preceded the post-burst. All three of these events had several characteristics in common; their typical evolution could be described as follows. Before the onset of the burst the active region would consist of several distinct sources of S-component radio emission. One or more of these sources would brighten, reaching a peak flux in less than 30 minutes. If more than one source brightened, the time profiles of each source's flux didn't coincide. The polarization percentage of each source remained nearly constant throughout the event. During the latter phases of the event, a diffuse source of unpolarized emission would appear with a diameter of several arc-minutes. The total duration of each event was an hour or longer.

There appears to be two distinct types of emission responsible for each of these events. The brightening of the pre-existing sources is one type of emission and it is probably caused by an enhancement of the solar S-component radiation. The diffuse source of unpolarized emission is the other type. The solar S-component emission is generally thought to be caused by gyro-resonance emission, which is thermal bremsstrahlung in the

presence of a sufficiently intense magnetic field (Kundu, 1965; Zheleznyakov, 1970). The emission occurs in the gyro-resonance levels above sunspots, and its intensity is proportional to the electron temperature in the gyro-resonance levels. The diffuse source of unpolarized radiation could be caused by thermal bremsstrahlung.

We propose the following model to explain our observations of the post-burst events. Initially a solar flare heats a small region of the solar atmosphere. The electrons accelerated by the flare process radiate the radio emission associated with a simple burst. The small heated region expands due to gas pressure and conduction, and at the same time its temperature is decreasing because of radiation losses and heating of the adjoining atmosphere. The heated region will radiate electromagnetic emission primarily by thermal bremsstrahlung. This emission would be observed as an expanding unpolarized radio source.

If the heated region's expansion should intersect a gyro-resonance emission layer, the gyro-resonance emission would increase proportional to the increase in temperature in the emission layer. As the heated region continued to cool, the gyro-resonance emission would gradually decrease to its pre-burst intensity. The expected effect would then be a rapid increase in the gyro-resonance emission as the heated region intersects the gyro-resonance emission layers, and then a slower decline as the heated region continues to cool. If more than one gyro-resonance source is present, each should show a different intensity profile since it is unlikely that the heated region's expansion would reach each source at the same time.

This model is in general agreement with the soft X-ray observations of solar flares. Horan (1970) and Kahler et al. (1970) have calculated

the temperature and emission measure for a number of X-ray flares, assuming that the X-ray emission is radiating from an isotropic plasma. The emission measure is defined as the (electron density) x (ion density) integrated over the volume of the plasma. In each of the events which they report on, the temperature reaches a maximum near the beginning of the X-ray flare before the peak X-ray flux. The temperature then begins a slow decay. The peak emission measure doesn't occur until after the peak flux, and in a number of events the emission measure was still increasing at the end of the event. In most events the emission measure increased one to two orders of magnitude. The most likely way for the emission measure to increase is for the plasma to heat the surrounding gas by conduction. This would increase the volume and decrease the temperature. This is the same sort of effect we propose in the model to explain the post-burst radio observations.

Felli et al. (1975) have calculated the expected radio flux for the 2 September 1973 event using the X-ray temperature and emission measure, assuming that all of the radio emission is radiating by thermal bremsstrahlung. They find that the measured radio flux is 2-4 times greater than the expected flux. Furthermore, their measured radio flux is at least a factor of 2 too low, since the interferometer was pointed 4' south of the burst location. This means that the measured radio flux is a factor of 4-8 greater than the predicted flux. However, Felli et al. (1975) didn't take into account the gyro-resonance emission from this active region. Comparing the pre-burst with the burst scans, it is clear that the gyro-resonance emission from the pre-existing sources is the dominant component during the burst. The measured and predicted thermal bremsstrahlung are probably in much closer agreement than Felli et al. (1975) indicated.

In conclusion, we believe that the centimeter post-burst emission is caused by two distinct emission mechanisms. The diffuse unpolarized emission is thermal bremsstrahlung and the enhanced S-component is gyroresonance emission. The time evolution of the post-burst emissions can be explained qualitatively by a small hot region heated during a solar flare, and then expanding as it cools.

7. RECOMMENDATIONS FOR FUTURE WORK

The Stanford interferometer was used to observe the sun for more than 400 hours during the period of this contract. During this time only 4 radio bursts were observed; this is a rate of roughly one radio burst per 100 hours of active region observations. Since the interferometer is limited to observing one active region at a time, the rate reflects the likelihood of a burst occurring in a selected active region, and it could possibly be improved by better selection of active regions.

The basic limitation of this work is the lack of radio bursts. Four bursts is too small a sample from which to make firm conclusions. With proper funding the Stanford interferometer could obtain more than 1000 hours of solar observing per year, and thus would observe many additional microwave bursts. This type of program would also allow the evolution of the solar microwave emission to be studied.

Secondly, the burst data should be obtained with better time resolution. Presently, the Stanford instrument is limited to 20 seconds per measurement without polarization, and 3 minutes with circular polarization. The latter interval has been insufficient to resolve a simple burst from a post-burst, which is important for determining the feasibility of the model presented in the previous section. Simple changes

to the interferometer would allow measurements with no polarization to be made in less than 5 seconds, and with circular polarization in less than 10 seconds.

Two-dimensional resolution of the radio bursts would be very desirable. However, it is unlikely that new instruments with this capability, such as the VLA, will be useful for this purpose due to the limited observing time available.

In conclusion, high resolution measurements of selected active regions should be made on a regular basis in the centimeter radio region. These measurements should have a spatial resolution of much less than $1''$, a time resolution of less than 1 minute, and the capability of detecting circular polarization. The measurements should be oriented to detecting microwave radio bursts when they occur. A better understanding of the origin of the microwave radio burst could lead to significant insight into the solar flare process.

REFERENCES

- Allen, C.W., (1964), Astrophysical Quantities, The Athlone Press, London.
- The American Ephemeris and Nautical Almanac, Superintendent of Documents, U.S. Government Printing Office, Washington, D.C.
- Bracewell, R.N., R.S. Colvin, L.R. D'Addario, C.J. Grebenkemper, K.M. Price, and A.R. Thompson, (1973), Proceedings of the IEEE, 16, 1249.
- D'Addario, L.R., (1974), "The Stanford Synthesis Radio Telescope: Theory, Calibration, and Data Processing; and a Study of Galactic H II Regions," Ph.D. Thesis, Stanford University.
- Explanatory Supplement to the Ephemeris, (1961), Her Majesty's Stationery Office, London.
- Felli, M., R. Pallavicini, and G. Tofani, (1975), Solar Physics, 44, 135.
- Horan, D.M., (1970), "Coronal Electron Temperatures Associated with Solar Flares," Ph.D. Dissertation, Catholic University.
- Kahler, S.W., J.F. Meekins, R.W. Kreplin, and C.S. Bowyer, (1970), Astrophysical Journal, 162, 293.
- Kundu, M.R., (1964), Solar Radio Astronomy, Chap. 7, John Wiley & Sons, New York.
- Kundu, M.R., R.H. Becker, and T. Velusamy, (1974), Solar Physics, 34, 187.
- Lang, K.R., (1974), Solar Physics, 36, 351.
- Morris, D., V. Radhakrishnan, and G.A. Seielstad, (1964), Astrophysical Journal, 139, 551.
- Ponsonby, J.E.B., (1973), Mon. Not. R. Astr. Soc., 163, 369.
- Wernecke, S.J., and L.R. D'Addario, (1976), to appear in IEEE Trans. Computers.
- Woolard, E.W., and G.M. Clemence, (1966), Spherical Astronomy, Academic Press, New York.
- Zheleznyakov, V.V., (1970), Radio Emission of the Sun and Planets, Pergamon Press, Oxford.

FILM
4

